

GLOBAL AND SEASONAL EFFECTS OF  
LIGHTNING-INDUCED ELECTRON PRECIPITATION

A DISSERTATION  
SUBMITTED TO THE COMMITTEE ON GRADUATE STUDIES  
OF STANFORD UNIVERSITY  
IN PARTIAL FULFILLMENT OF THE REQUIREMENTS  
FOR THE DEGREE OF  
DOCTOR OF PHILOSOPHY  
IN  
ELECTRICAL ENGINEERING

Austin Patrick Sousa  
January 2018

© Copyright by Austin Patrick Sousa 2018

All Rights Reserved

I certify that I have read this dissertation and that, in my opinion, it is fully adequate in scope and quality as a dissertation for the degree of Doctor of Philosophy.

---

(Prof. Sigrid Close) Principal Adviser

I certify that I have read this dissertation and that, in my opinion, it is fully adequate in scope and quality as a dissertation for the degree of Doctor of Philosophy.

---

(Prof. Robert Marshall, University of Colorado Boulder)

I certify that I have read this dissertation and that, in my opinion, it is fully adequate in scope and quality as a dissertation for the degree of Doctor of Philosophy.

---

(Prof. Antony Fraser-Smith)

Approved for the Stanford University Committee on Graduate Studies

---

# Preface

This thesis tells you all you need to know about...

# Acknowledgments

(Acknowledgements go here)

# Contents

<b>Preface</b>	<b>iv</b>
<b>Acknowledgments</b>	<b>v</b>
<b>1 Introduction</b>	<b>1</b>
1.1 The Space Environment . . . . .	1
1.2 Motivation . . . . .	2
1.3 Previous Work . . . . .	2
1.4 Thesis Organization . . . . .	2
<b>2 Physics and Methods</b>	<b>3</b>
2.1 Overview of Plasma Physics . . . . .	3
2.1.1 Single Particle Motion . . . . .	4
2.1.2 The Loss Cone . . . . .	7
2.1.3 Waves in Plasmas . . . . .	9
2.2 Lightning Illumination Model . . . . .	15
2.3 The Ionosphere . . . . .	16
2.3.1 Trans-Ionosphere Attenuation . . . . .	16
2.3.2 Models of the Ionosphere . . . . .	19
2.4 The Earth's magnetic field . . . . .	21
2.4.1 Models of the magnetic field . . . . .	21
2.5 The Plasmasphere . . . . .	23
2.5.1 Ray Tracing . . . . .	27
2.5.2 Landau Damping . . . . .	30

2.6	The Radiation Belts . . . . .	32
2.7	Wave-Particle Interactions . . . . .	36
2.7.1	Resonant Interactions . . . . .	36
2.7.2	Recovering Wave Amplitudes from Poynting Flux . . . . .	39
2.8	The GLD360 Lightning Dataset . . . . .	40
<b>3</b>	<b>VLF energy in the Near-Earth Environment</b>	<b>44</b>
3.1	Methodology . . . . .	44
3.2	Persistent Energy from a Single Flash . . . . .	45
3.2.1	Radiated power above the ionosphere . . . . .	45
3.2.2	Gridding and Interpolation . . . . .	47
3.2.3	Energy imparted by a single flash . . . . .	54
3.3	Global Energy Density . . . . .	54
3.3.1	Results of the global model . . . . .	58
<b>4</b>	<b>3D Modeling of LEP</b>	<b>63</b>
4.1	Selection of a Canonical Lightning Flash . . . . .	63
4.2	Pseudo-3D vs Scaled 2D . . . . .	63
4.3	Geometric Factor . . . . .	63
<b>5</b>	<b>Global and Seasonal Estimates of LEP</b>	<b>64</b>
5.1	LEP stencils . . . . .	64
5.2	Coordinate deformation . . . . .	64
5.3	Global and Seasonal Energy Fluxes . . . . .	66
5.4	Lifetime Estimates . . . . .	66
<b>6</b>	<b>Satellite Instrumentation for LEP Measurement</b>	<b>67</b>
6.1	VPM Mission Overview . . . . .	67
6.2	Hardware Architecture . . . . .	67
6.2.1	Wave Measurement . . . . .	67
6.2.2	Particle Measurement . . . . .	67
6.3	Firmware Architecture . . . . .	67

<b>7 Conclusions</b>	<b>68</b>
7.1 Suggestions for Future Work . . . . .	68
<b>A Reference Equations</b>	<b>69</b>
A.1 Landau Damping . . . . .	69
<b>B Runge-Kutta Methods</b>	<b>72</b>
<b>Bibliography</b>	<b>73</b>

# List of Tables

3.1 Simulation Parameters . . . . .	46
-------------------------------------	----

# List of Figures

2.1	An example of a “magnetic bottle” particle trap . . . . .	6
2.2	Adiabatic motion in the Earth’s magnetic field . . . . .	8
2.3	Loss cone illustration . . . . .	9
2.4	An $\omega$ -K diagram for the cold, four-component dispersion relation, for parallel propagation at $L \approx 3$ . . . . .	14
2.5	Time and frequency profiles of the lightning illumination model . . .	17
2.6	Trans-Ionosphere attenuation curves for day and night . . . . .	20
2.7	Ionosphere density profile . . . . .	21
2.8	Magnetic field models . . . . .	24
2.9	L-shell contours on the Earth’s surface . . . . .	25
2.10	Model of plasmapause location . . . . .	26
2.11	A Comparison of three plasmasphere electron density models . . . .	28
2.12	Example ray tracing . . . . .	30
2.13	Phase-space density functions . . . . .	33
2.14	AE8 integral flux model . . . . .	34
2.15	Pitch-angle distribution functions . . . . .	35
2.16	Illustration of resonant wave-particle interactions . . . . .	37
2.17	Average global flash rate . . . . .	42
2.18	Average global peak current rate rate . . . . .	43
3.1	Energy density calculation block diagram . . . . .	45
3.2	Illumination pattern below the ionosphere . . . . .	47
3.3	Illumination pattern above the ionosphere . . . . .	48
3.4	Energy above the ionosphere due to a single flash . . . . .	49

3.5	Illustrations of the interpolation scheme . . . . .	50
3.6	Delaunay interpolation method . . . . .	51
3.7	Fine-scale frequency interpolation . . . . .	52
3.8	Illustration of a convex hull in two dimensions. (a) A simple polygon, shown in orange, for which the convex hull and concave hulls differ substantially. (b) A collection of random points, and their concave hull.	53
3.9	Block diagram . . . . .	55
3.10	Energy density vs time vs L-shell . . . . .	56
3.11	Energy density stencils . . . . .	57
3.12	Average energy density vs longitude and L . . . . .	60
3.13	Average energy density vs L, longitude-averaged . . . . .	61
3.14	Average energy density vs L for multiple $K_p$ . . . . .	61
3.15	Average energy density vs L and frequency . . . . .	62
5.1	Comparison of Magnetic Dipole (MAG) and Corrected Geomagnetic (CGM) coordinates . . . . .	66

# Chapter 1

## Introduction

### 1.1 The Space Environment

Surrounding the Earth there exists a sparse gas of ions and electrons called a *plasma*. These particles reside in a state of constant flux, resulting from a tenuous and dynamic balance of energy fluxes – streaming in from the sun, and back and forth within the Earth’s terrestrial atmosphere. Every human-made satellite has passed through it; the vast majority of satellites, with the exception of deep-space probes, live out their entire existence within it. Aside from the lunar astronauts of the Apollo era, every single human in space has spent the duration of their journey within this constantly-evolving cloud of matter. The technology ubiquitous in our day-to-day lives – instant international communication, satellite-aided global positioning systems – all require signals to be transmitted through it. We call this region, from say, an altitude of 100 km on out to the moon, the *Space Environment*.

## 1.2 Motivation

## 1.3 Previous Work

## 1.4 Thesis Organization

The bulk of this thesis is divided into the following chapters.

- Chapter 2 describes the background physics of the LEP process, the numerical methods used within this study, and the mathematical models of the various environments which we examine.
- Chapter 3 presents a study of the persistent VLF radio energy within the magnetosphere, resulting from terrestrial cloud-to-ground lightning discharges.
- Chapter 4 provides a simulation of electron precipitation resulting from a canonical cloud-to-ground lightning discharge, and a discussion of various model improvements, notably with our treatment of the longitudinal axis.
- Chapter 5 provides seasonal estimates of the global impact of LEP resulting from the GLD360 dataset and a reduced-complexity model.
- Chapter 6, admittedly a bit of a tangent, presents the design of a CubeSat-based instrumentation suite, designed for direct, *in-situ* measurements of LEP by taking time-and-space-coincident measurements of electron loss cone distributions, and incident VLF waves. The design provides some interesting on-board signal processing to reduce the data bandwidth significantly, and is implemented entirely in fixed-point logic using an FPGA (and *no* onboard CPU). I worked on this design in the earlier years of my time at Stanford; at time of writing it is due to be launched in early 2019.

# Chapter 2

## Background Physics and Description of Methods

### 2.1 Overview of Plasma Physics

A *plasma* is a quasi-neutral gas of ions, electrons, and neutral particles, which exhibit collective behavior. Plasmas can behave in similar ways to a conventional fluid – they can flow, they can be compressible, they can be turbulent, and so on – however the addition of charged particles facilitates many behaviors unique to a plasma. Charged particles can interact with each other not just through ballistic collisions, but at a distance through electromagnetic forces. The bulk motion of a plasma can be manipulated through electric and magnetic fields; conversely a plasma can have a substantial effect on the propagation of radio waves passing through it.

A plasma can be analyzed in several different domains: Single particle motion; fluid approximations; and full kinematic solutions. In this work we treat the motions of electrons in the single particle domain, which is a natural choice for the sparse densities and small gyroradii of radiation belt electrons. To understand the behavior of radio waves propagating through a plasma, we treat the background as a smooth dielectric medium.

### 2.1.1 Single Particle Motion

The high energies and sparse densities of the radiation belts lend themselves very well to a single-particle approximation. Many of the basic behaviors and quantities in plasma physics can be understood through studying the motion of a single particle.

The fundamental equation of motion for a charged particle in an electromagnetic field is given by the Lorentz force:

$$\mathbf{F} = \frac{d\mathbf{p}}{dt} = q(\mathbf{E} + \mathbf{v} \times \mathbf{B}) \quad (2.1)$$

Where  $q$  represents the particle's charge,  $\mathbf{E}$  and  $\mathbf{B}$  represent the electric and magnetic fields, and  $\mathbf{v}$  the particle's velocity, shown here in a non-relativistic frame.

Electric fields simply apply a force in the direction of the field. However, note that a cross product is perpendicular to both terms – therefore any forces induced by the magnetic field will be perpendicular to the particle's velocity. The magnetic field is a *conservative* force, in that a stationary magnetic field cannot directly impart energy into a particle, but can alter a particle's trajectory. The particle will therefore have a net drift in the direction of the electric field, while exhibiting a helical motion around the magnetic field.

We can then split the velocity vector into two quantities –  $v_{\parallel}$  parallel to the magnetic field, and  $v_{\perp}$  perpendicular to the magnetic field. Two characteristic values arise from this motion: the radius of the particle's rotation around the magnetic field, known as the *gyroradius* or the *Larmor radius*:

$$r_l = \frac{mv_{\perp}}{qB} \quad [\text{m}] \quad (2.2)$$

and the rotation frequency, known as the *gyrofrequency* or *cyclotron frequency*:

$$\omega_c = \frac{v_{\perp}}{r_l} = \frac{qB}{m} \quad [\text{rad/sec}] \quad (2.3)$$

By integrating the particle's momentum over a single gyrorotation, we arrive at a third fundamental quantity known as the magnetic moment, or the *first adiabatic*

*invariant:*

$$\mu = \frac{mv_{\perp}^2}{2B} \quad (2.4)$$

In situations where the magnetic field varies slowly (e.g., on spatial scales much greater than the gyroradius),  $\mu$  remains a constant of motion.

A final parameter to describe a particle's motion is its *pitch angle*, the angle between the velocities perpendicular and parallel to the magnetic field:

$$\alpha = \tan^{-1}\left(\frac{v_{\perp}}{v_{\parallel}}\right) \quad (2.5)$$

The first adiabatic invariant describes an implicit relationship between the magnetic field strength and a particle's pitch angle at a given point. Combining the first adiabatic invariant with conservation of kinetic energy, we can deduce an expression for magnetic trapping – that is, the magnetic field strength in which a particle exhibiting helical motion along a magnetic field line will turn around.

$$E = \frac{1}{2}mv^2 \quad (2.6)$$

$$= \frac{1}{2}m(v_{\parallel}^2 + v_{\perp}^2) \quad (2.7)$$

$$= \frac{1}{2}mv^2(\cos^2\alpha + \sin^2\alpha) \quad (2.8)$$

At a reflection point, the particle's kinetic energy will be entirely in the perpendicular mode:

$$\frac{v_{\perp 0}^2}{B_0} = \frac{v_{\perp 1}^2}{B_1} \quad (2.9)$$

$$\frac{v^2 \sin^2(\alpha)}{B_0} = \frac{v^2}{B_1} \quad (2.10)$$

$$\sin^2(\alpha) = \frac{B_0}{B_1} \quad (2.11)$$

A charged particle in a magnetic field will therefore be constrained to rotate around a field line, and feel an opposing longitudinal force as the field intensity increases.

If the magnetic field is such that there are two regions of increasing intensity, separated by a reasonable distance, the particle may bounce back and forth, reflecting at turning points given by equation 2.11. Such a field configuration is known as a “magnetic bottle” particle trap, as shown in figure 2.1. A key observation is that the reflection point is independent of energy, and depends only on the ratio of magnetic field strengths and the particle’s initial pitch angle.

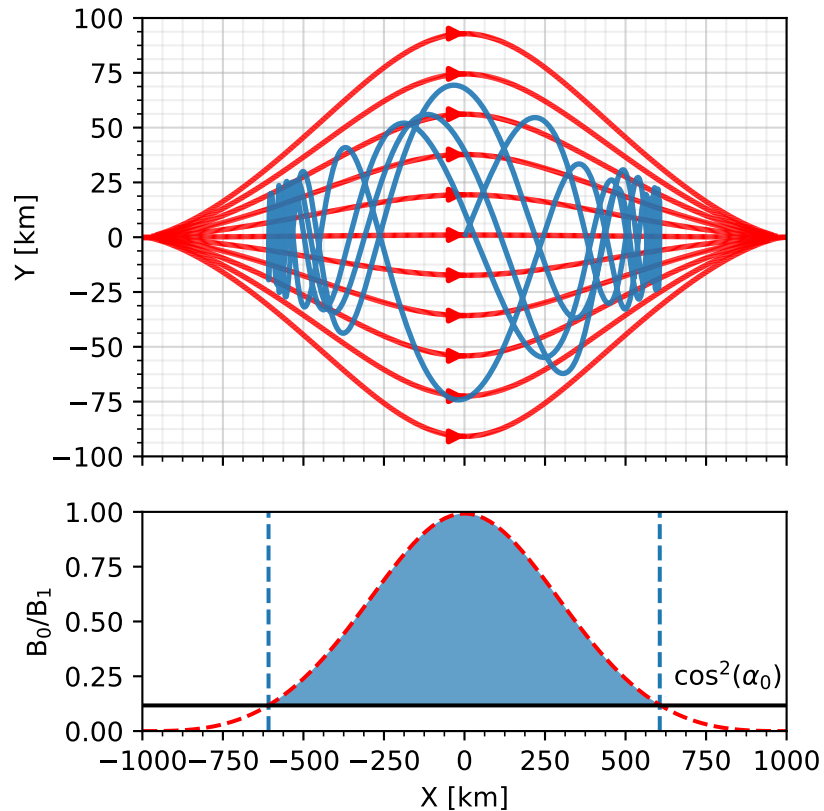


Figure 2.1: An example of a “magnetic bottle” particle trap. The top plot shows the trajectory of an electron with an initial pitch angle  $\alpha_0 = 20^\circ$ . The bottom plot shows the magnetic field ratio  $B_0/B_1$ , with the particle’s reflection points shown as vertical lines.

### 2.1.2 The Loss Cone

A magnetic bottle trap need not be linearly-arranged, as it is in figure 2.1; we require only that the magnetic field be slowly-varying with respect to the particle's gyroradius. The Earth's dipole magnetic field forms a natural and effective particle trap, which dominates the morphology of charged particle populations surrounding the Earth. The motion of a charged particle in the Earth's magnetic field can be broken into three components (see figure 2.2):

- a rapid gyrorotation around the background magnetic field
- a “bouncing” motion between the north and south poles, with periods ranging from milliseconds to several seconds; and
- a slower, longitudinal drift, causing the particles to precess around the earth on the order of minutes to days, resulting from the magnetic field gradient

We can average the particle's motion over a single gyrorotation to define a *guiding center*, the trajectory of which follows the background magnetic field line.

As described previously, a trapped particle's reflection points are defined by the particle's initial pitch angle, and the strength of the magnetic field. In the case of the Earth, however, these turning points are limited in feasibility as well – for instance, a particle naturally cannot have a reflection point lower than the Earth's surface. Moreover, the Earth's neutral atmosphere becomes exponentially more-dense with decreasing altitude; particles reflecting at an altitude below  $\approx 100$  km will encounter a significant neutral molecule population, and stand a very good chance of colliding. A collision with atmospheric constituents can result in the particle losing some, or all, of its kinetic energy through ionization, and may be completely lost from the system, or return onto a different fieldline, with a different energy and/or pitch angle (Cotts, 2011).

With an understanding of the dense neutral atmosphere, we can define a critical altitude – 100 km here and in previous work – and thus a critical pitch angle, known

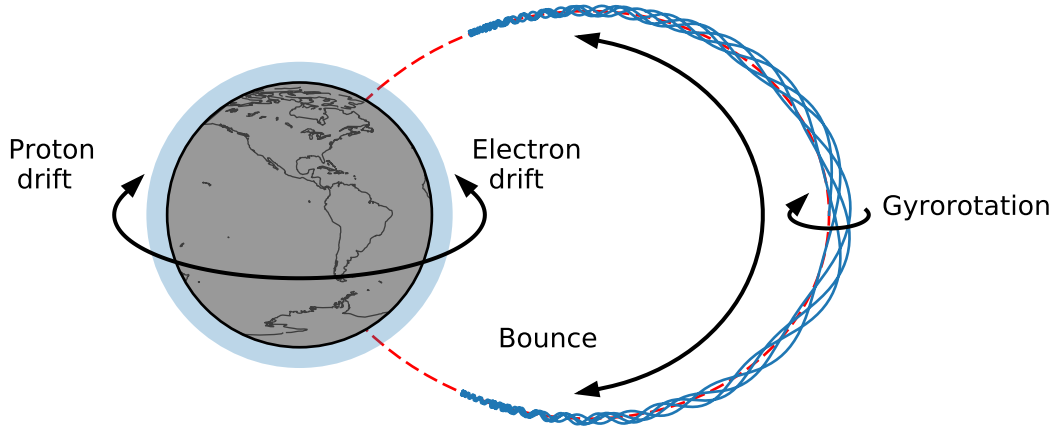


Figure 2.2: Illustration of the various motions exhibited by a charged particle in the Earth’s magnetic field

as the (bounce) *loss-cone angle*:

$$\sin \alpha_{lc} = \sqrt{\frac{B(\mathbf{r})}{B_{h_m}}} \quad (2.12)$$

where  $h_m$  is the reflection height, and  $B(\mathbf{r})$  is measured at the reference point – either the particle’s current location for a *local loss cone angle*, or at the equator along the field line for the *equatorial loss cone angle*.

In the case of a dipole magnetic field model, we can determine the equatorial loss cone explicitly:

$$\sin \alpha_{lc} = \sqrt{\frac{\zeta_m^3}{\sqrt{1 + 3(1 - \zeta_m)}}} \quad \zeta_m = (R_e + h_m)/(LR_e) \quad (2.13)$$

where  $R_e = 6371$  km is the radius of the Earth, and L is the *L-shell* of interest (see

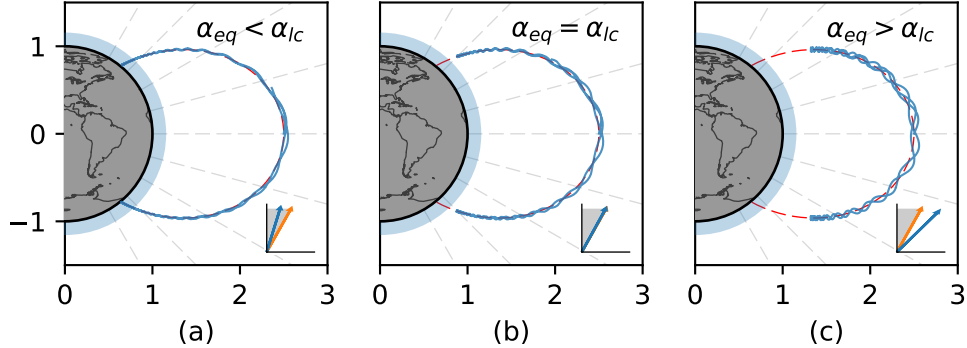


Figure 2.3: An illustration of the loss cone. The trajectory of a test electron is shown in blue, for three different equatorial pitch angles: (a) a precipitating particle with a pitch angle within the loss cone, (b) at the edge of the loss cone, and (c), a stably-trapped particle with a pitch angle well outside the loss cone.

section 2.4.1).

**Bounce and Drift Loss Cones** We have discussed what is known as the *bounce loss cone*. Also of interest in the study of the space environment is the *drift loss cone*. The drift loss cone is the largest loss cone along the same L-shell, as it varies longitudinally. Conceptually, as a particle drifts longitudinally, it may encounter a different loss cone, and could precipitate at certain longitudes, but not others. At some point along this longitudinal precession, the particle will encounter the maximum bounce loss cone, and precipitate (see *Cotts (2011)*, figure 2.3).

Under a simple dipole magnetic field model, the bounce loss cone is uniform around the globe, and the bounce and drift loss cones are identical. Within this dissertation, we primarily work with a dipole magnetic field model, and consider only the bounce loss cone.

### 2.1.3 Waves in Plasmas

Previously, we have described the motion of a charged particle under the influence of an electromagnetic field. the single-particle approximation provides enormous insight

into the dynamics of a sparsely-populated plasma. Next, we must consider the inverse system: how the charged particles in a plasma dictate the characteristic behaviors of an electromagnetic wave propagating through it.

An electromagnetic wave can accelerate a charged particle; conversely, an accelerating or decelerating particle induces its own electromagnetic field. It would seem, then, that the behavior of an electromagnetic field in a plasma is simply the summation of the contributions of each particle and some incident wave source. However, the complexity of this brute-force approach quickly becomes intractable for even a handful of particles. The universal approach taken then is to abstract the complicated interplay of waves and particles into a wave moving through a dielectric medium, described only by the various constituent densities, temperatures, and background fields within a given volume.

As with any electromagnetic problem, we begin with Maxwell's equations, shown here in their non-relativistic, differential form, in SI units:

$$\nabla \cdot \mathbf{E} = \frac{\rho}{\epsilon_0} \quad (2.14)$$

$$\nabla \cdot \mathbf{B} = 0 \quad (2.15)$$

$$\nabla \times \mathbf{E} = -\frac{\partial \mathbf{B}}{\partial t} \quad (2.16)$$

$$\nabla \times \mathbf{B} = \mu_0 \mathbf{J} + \frac{1}{c^2} \frac{\partial \mathbf{E}}{\partial t} \quad (2.17)$$

$\mathbf{E}$  and  $\mathbf{B}$  denote the electric and magnetic fields;  $\mu_0$  and  $\epsilon_0$  denote the magnetic permeability and electric permittivity of free space; and  $c = \sqrt{\frac{1}{\mu_0 \epsilon_0}}$  is the speed of light in vacuum. The terms  $\rho$  and  $\mathbf{J}$  represent the local charge density and current density, both of which may be functions of position and time.

By taking the curl of equation 2.16 and substituting in the time derivative of equation 2.17, and making use of the vector identity  $\nabla \times \nabla \times \mathbf{E} = \nabla(\nabla \cdot \mathbf{E}) - \nabla^2 \mathbf{E}$ , we have:

$$\nabla^2 \mathbf{E} - \frac{\nabla \rho}{\epsilon_0} = \mu_0 \frac{\partial \mathbf{J}}{\partial t} + \frac{1}{c^2} \frac{\partial^2 \mathbf{E}}{\partial t^2} \quad (2.18)$$

In the absence of charges or currents ( $\rho = 0, \partial\mathbf{J}/\partial t = 0$ ), the equation reduces to the free-space wave equation:

$$\nabla^2\mathbf{E} = \frac{1}{c^2} \frac{\partial^2\mathbf{E}}{\partial t^2} \quad (2.19)$$

Next, we search for harmonic perturbations of the form:

$$\mathbf{E}(\mathbf{r}, t) = \mathbf{E}_1 e^{i(\omega t - \mathbf{k} \cdot \mathbf{r})} \quad (2.20)$$

$$\mathbf{B}(\mathbf{r}, t) = \mathbf{B}_0 + \mathbf{B}_1 e^{i(\omega t - \mathbf{k} \cdot \mathbf{r})} \quad (2.21)$$

$$\mathbf{J}(\mathbf{r}, t) = \mathbf{J}_1 e^{i(\omega t - \mathbf{k} \cdot \mathbf{r})} \quad (2.22)$$

where  $\omega$  is the wave angular frequency,  $\mathbf{k}$  is the wave vector, or spatial frequency, and  $\mathbf{r}$  is the spatial coordinate. Two fundamental parameters of an electromagnetic wave are the *phase velocity*,  $\omega/k$ , and the *group velocity*,  $\partial\omega/\partial k$ . The relation between the temporal and spatial frequencies is known as the *dispersion relation*.

From here we follow the derivation and convention used by *Stix* (1992) and *Bitencourt* (2004). In general, a plasma is comprised of several different species of constituent particles – positively and negatively charged particles necessary to maintain a quasi-neutral plasma. While the dispersion relations of different species cannot be simply added, their effects can be summed to form the displacement current  $\mathbf{J}$ :

$$\mathbf{J} = \sum_s \mathbf{J}_s = \sum_s n_s q_s \mathbf{u}_s \quad (2.23)$$

where  $n$ ,  $q$ , and  $\mathbf{u}$  represent the (number) density, charge, and velocity of a particular species  $s$ .

We make the assumption that the plasma is *cold* – that is, that all particles of a particular species are moving with the same velocity  $\mathbf{u}_s$ , with no thermal variation. Were we to relax this assumption, each species density would have a distribution function in both position and momentum,  $n = n(\mathbf{r}, \mathbf{p})$ ; the total current would then be an integration over momentum for each species. For a treatment of a hot plasma, see the work by *Sazhin* (1993).

Next, we note that, in a cold plasma assumption, the Lorentz force (equation 2.1)

can be written for each species:

$$m_s \frac{d\mathbf{u}_s}{dt} = q_s (\mathbf{E} + \mathbf{u}_s \times \mathbf{B}) \quad (2.24)$$

Combining equations 2.20 – 2.22, 2.23, and 2.24, and assuming a coordinate system with the background magnetic field  $\mathbf{B}_0$  aligned with the z-axis, we arrive at an expression for the *cold-plasma dielectric tensor*:

$$\boldsymbol{\epsilon} \cdot \mathbf{E} = \begin{pmatrix} S & -iD & 0 \\ iD & S & 0 \\ 0 & 0 & P \end{pmatrix} \begin{pmatrix} E_x \\ E_y \\ E_z \end{pmatrix} \quad (2.25)$$

The various summations over each constituent species are incorporated into the so-called Stix parameters (*Stix (1992)*):

$$S = \frac{1}{2}(R + L) \quad D = \frac{1}{2}(R - L) \quad (2.26)$$

$$R = 1 - \sum_s \frac{\omega_{ps}^2}{\omega(\omega + \omega_{cs})}; \quad L = 1 - \sum_s \frac{\omega_{ps}^2}{\omega(\omega - \omega_{cs})}; \quad P = 1 - \sum_s \frac{\omega_{ps}^2}{\omega^2} \quad (2.27)$$

where  $\omega_{ps} = n_s q_s^2 / \epsilon_0 m_s$  and  $\omega_{cs} = q_s B_0 / m_s$  are the plasma and cyclotron frequencies for species  $s$ .

### Dispersion Relation

With the dielectric tensor now determined, we can derive the relationship between  $\omega$  and  $\mathbf{k}$ , known as the dispersion relation. Equation 2.18 can be written as:

$$\boldsymbol{\eta} \times \boldsymbol{\eta} \times \mathbf{E} + \boldsymbol{\epsilon} \cdot \mathbf{E} = 0 \quad (2.28)$$

where  $\eta = \mathbf{k}c/\omega$  is the wave refractive index. Assuming a wave propagating with some angle  $\theta$  between  $\eta$  and the background magnetic field, we arrive at:

$$\begin{pmatrix} S - \eta^2 \cos^2 \theta & -iD & \eta^2 \cos \theta \sin \theta \\ iD & S - \eta^2 & 0 \\ \eta^2 \cos \theta \sin \theta & 0 & P - \eta^2 \sin^2 \theta \end{pmatrix} \begin{pmatrix} E_x \\ E_y \\ E_z \end{pmatrix} = 0 \quad (2.29)$$

Taking the determinant of 2.29 yields the *cold-plasma dispersion relation*:

$$A\eta^4 - B\eta^2 + C = 0 \quad (2.30)$$

$$A = S \sin^2 \theta + P \cos^2 \theta \quad (2.31)$$

$$B = RL \sin^2 \theta + PS(1 + \cos^2 \theta) \quad (2.32)$$

$$C = PRL \quad (2.33)$$

Equation 2.30 is biquadratic – we can solve for  $\eta^2 = k^2 c^2 / \omega^2$  using the quadratic formula.

Finally, it is worth noting that when considering a single-species plasma (e.g., electrons only), equation 2.30 reduces to the well-known single-species *Appleton-Hartree Equation* (Appleton (1932)):

$$\eta^2 = 1 - \frac{\frac{\omega_{pe}^2}{\omega^2}}{1 - \frac{\omega_{ce}^2 \sin^2 \theta}{2(\omega^2 - \omega_{pe}^2)} \pm \left[ \left( \frac{\omega_{ce}^2 \sin^2 \theta}{2(\omega^2 - \omega_{pe}^2)} \right)^2 + \frac{\omega_{ce}^2}{\omega^2} \cos^2 \theta \right]^{1/2}} \quad (2.34)$$

The dispersion relation in equation 2.30 reveals a wealth of information about the characteristics of waves in plasmas. For various plasma densities and background magnetic field strength, we can infer which wave frequencies may propagate, if any, and which wave polarizations. Through the remainder of this work, we will be concerned with the *whistler* mode – a right-hand, circularly-polarized (RHCP) wave. Within a typical magnetospheric plasma, the whistler mode spans the VLF band, roughly between 30 Hz and 300 kHz.

It is difficult to gain much insight directly from the dispersion relation (equations 2.30 or 2.34). However, we can plot the spatial vs temporal frequencies for a fixed angle with respect to the background magnetic field, known as an  $\omega$ -K diagram, to reveal the various modes of propagation.

Figure 2.4 shows a typical dispersion relation for a magnetospheric plasma ( $L \approx 2$ ) by plotting frequency vs wavenumber ( $\eta = kc/\omega$ ). The whistler mode is the lower branch of the RHCP mode.

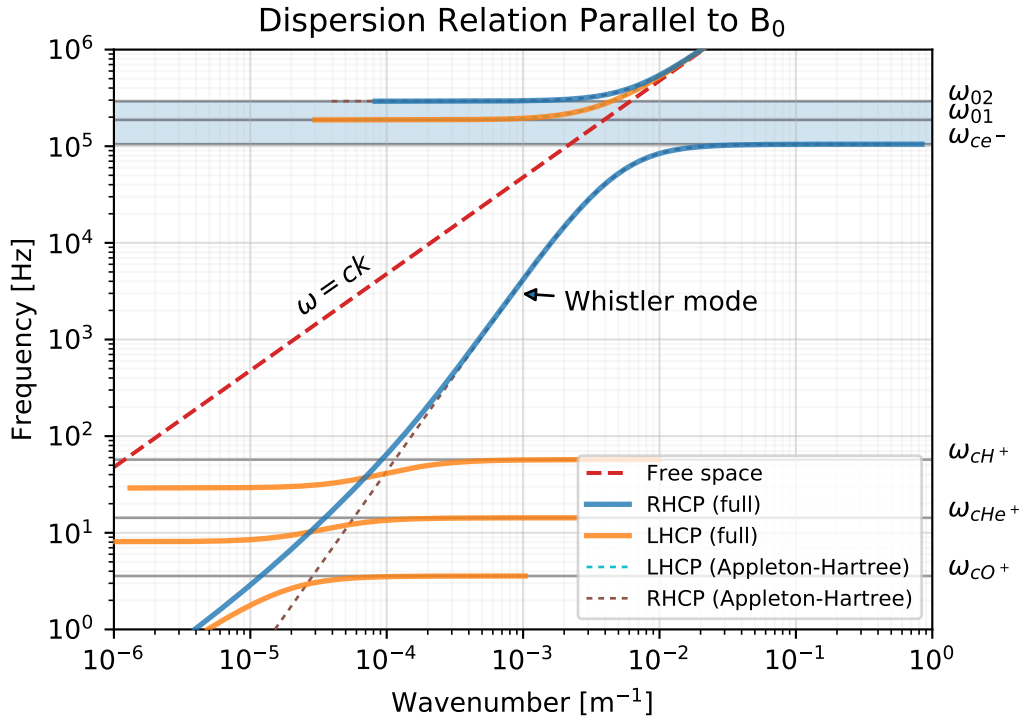


Figure 2.4: An  $\omega$ -K diagram for the cold plasma dispersion relation, shown here for a wave propagating parallel to  $\mathbf{B}$ , in four-component plasma with  $N_e \approx 6 \times 10^8 e^-/m^3$ , and  $B \approx 4 \mu T$ . For higher frequencies the dispersion relation asymptotes to the free-space solution, with slope  $c$ . The whistler mode is the right-hand, circularly-polarized mode which spans the majority of the frequency band. The shaded region marks the characteristic band in which the right-hand mode cannot propagate. At lower frequencies, the left-hand circular mode resonates with the various ion constituents, known as the *Ion Cyclotron* modes.

## 2.2 Lightning Illumination Model

A single lightning flash is a stochastic dielectric breakdown process. While a terrestrial lightning flash consists of several repeated strokes at varying incident angles, we adopt the simplified model used by *Lauben* (1998), *Bortnik* (2005), and subsequent workers, and encapsulate the entire discharge process in a single return stroke.

The lightning flash is modeled as a single, vertical current pulse from a height  $H_E$ , with a double-exponential time profile given by equation 2.35. The double-exponential current profile is simple and common in the literature, originating with *Bruce and Golde* (1941):

$$I(t) = I_0(e^{-at} - e^{-bt}) \quad (2.35)$$

We relate the time-domain current profile to radiated power using the far-field approximation for an arbitrary source, given by *Griffiths* (1999), page 457:

$$S(t) \frac{1}{\mu_0} (\mathbf{E} \times \mathbf{B}) = \frac{\mu_0}{16\pi^2 c} [\ddot{p}(t)]^2 \left( \frac{\sin^2 \theta}{r^2} \right) \hat{\mathbf{r}} \quad (2.36)$$

where  $p(t)$  is the dipole moment given by  $p = 2H_E \int_0^t I(t)dt$ ,  $r$  is the distance from the flash in meters, and  $\theta$  is the angle to the flash. Taking the second derivative of the dipole moment (the first derivative of the current profile) gives us the far-field time-domain power equation:

$$S(t) = \frac{1}{Z_0} \left( \frac{\mu_0 H_E I_0}{2\pi} \right)^2 \left( \frac{\sin^2 \theta}{r^2} \right) (ae^{-at} - be^{-bt})^2 \hat{\mathbf{r}} \quad (2.37)$$

where we have used the relation  $Z_0 = \mu_0 c$ . Equation 2.37 gives energy flux density in units of Watts per square meter ( $J/m^2/\text{sec}$ ).

To determine the frequency spectrum of the radiated power, we take the Fourier transform of equation 2.37:

$$S(\omega) = \frac{1}{Z_0} \left( \frac{\mu_0 H_E I_0}{2\pi} \right)^2 \left( \frac{\sin^2 \theta}{r^2} \right) \frac{\omega^2(a-b)^2}{\pi(\omega^2 + a^2)(\omega^2 + b^2)} \hat{\mathbf{r}} \quad (2.38)$$

which gives spectral energy flux, in units of  $J/m^2/\text{Hz}$ .

Throughout this work we assume a flash height  $H_E = 5$  km, and model parameters  $a = 5 \times 10^3$  sec $^{-1}$  and  $b = 1 \times 10^5$  sec $^{-1}$ , resulting in a spectrum peaked at approximately 4 kHz; any lightning flash can be parameterized solely by its peak current  $I_0$  and its location on the surface of the Earth. Figure 2.5 shows the current profile and associated spectrum.

The total energy released in a single discharge is determined by integrating equation 2.37 over time and a half-sphere surface:

$$E = \int_{t=0}^{\infty} \int_{\phi=0}^{2\pi} \int_{\theta=0}^{\pi} S(t) r^2 \sin \theta d\theta d\phi dt \quad (2.39)$$

$$= \frac{1}{Z_0} \left( \frac{\mu_0}{2\pi} \right)^2 \frac{(a-b)^2}{2(a+b)} \frac{4\pi}{3} H_e^2 I_0^2 \quad (2.40)$$

$$\approx 1.9 \times 10^{-14} H_e^2 I_0^2 \quad [\text{Joules}] \quad (2.41)$$

## 2.3 The Ionosphere

The ionosphere, extending from  $\approx 85$  km to 1000 km, is the highly-variable transition region between the terrestrial neutral atmosphere and the sparse plasmas of the space environment. The relatively-sharp rise in electron density at the bottom of the ionosphere makes it highly-reflective within the VLF band, forming a waveguide between it and the conductive surface of the Earth. However, In studying LEP, we are primarily concerned with the fraction of energy which does not reflect, and instead propagates through the ionosphere and out into the plasmasphere.

### 2.3.1 Trans-Ionosphere Attenuation

The ionosphere is a region of high variability, and a significant factor in the LEP process. As discussed earlier, the majority of VLF energy emitted by a lightning flash propagates efficiently in the Earth-Ionosphere waveguide; however a fraction of emitted energy can propagate upwards through the ionosphere, where the wave

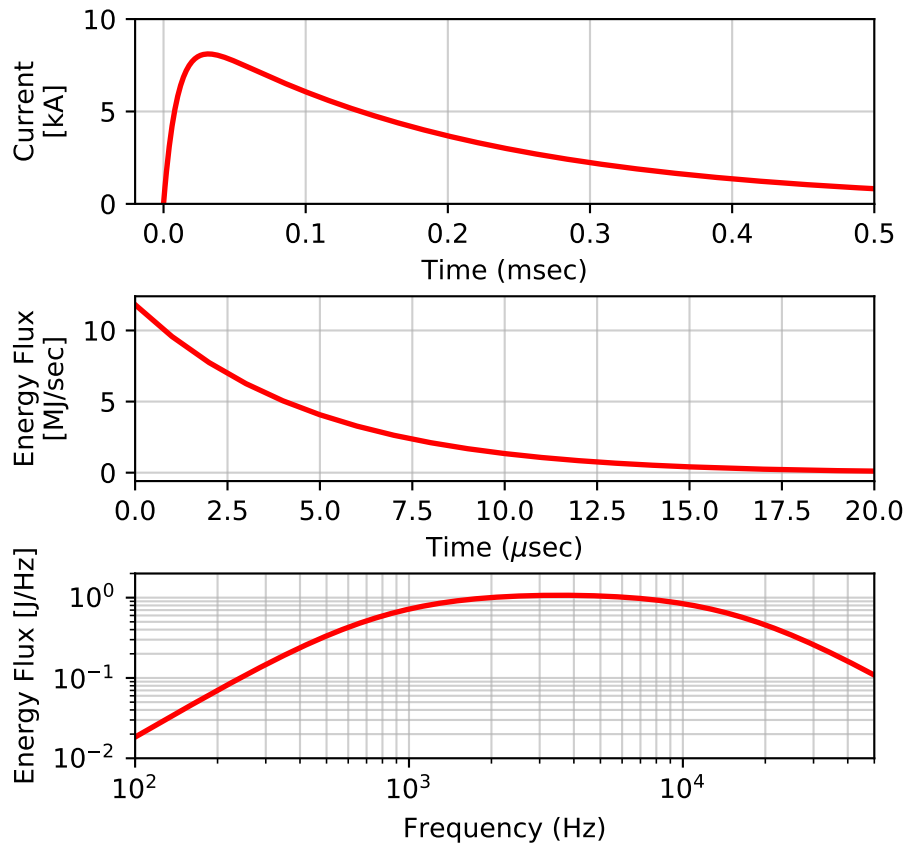


Figure 2.5: Double-exponential current pulse model of a lightning stroke. The top panel shows the stroke current vs time; the middle panel shows the total energy flux, integrated over space, vs time; the bottom panel shows the energy flux in the frequency domain.

experiences significant losses via Joule heating in the D-region ionosphere (*Graf et al.*, 2013; *Blaes et al.*, 2016).

Propagation through the ionosphere is ill-suited for a raytracing approach, as in section 2.5, for several reasons: first, the ionosphere electron density varies significantly across a relatively thin slab, effectively violating the WKB (smoothly-varying) approximation. Second, the Landau calculations used to compute ray damping are designed for warm, but collisionless plasmas; the ionosphere is collisional, and only partially ionized, requiring different treatment.

Ionospheric propagation is further complicated by reflection and transmission at the lower boundary layer, as well as mode-coupling between incident plane waves, the whistler mode, and various others.

For computational simplicity, and to more-easily generalize to a variety of conditions, we treat the ionosphere as a single absorbing slab, ranging from 100 to 1000 km in altitude. We assume that waves propagate directly upwards (normal to the Earth’s surface), and are not deflected by ionospheric irregularities or the inclination of the background magnetic field.

Numerous researchers (*Lauben*, 1998; *Bortnik*, 2005; *Kulkarni*, 2009; *Graf et al.*, 2013) have used the classic “Helliwell” curves, taken from *Helliwell* (1965), figure 3-35. Helliwell performs an analysis similar to Landau damping – first deriving a dispersion relation for a collisional plasma, then separating out the imaginary component, which will result in a real-valued attenuation term. The resulting attenuation term is dependent on electron density as a function of altitude, which was extrapolated from sounding rocket campaigns for day and night. The net attenuation is then computed by integrating from 65 to 1500 km in altitude.

Helliwell’s curves have persisted as the default record of trans-ionospheric attenuation; however it has been shown that Helliwell’s curves overestimate trans-ionosphere attenuation by 10 to 20 dB (*Starks et al.*, 2008), due mainly to the coarse measurement of the ionosphere electron density profile.

Rather than Helliwell’s curves, we use results from *Graf et al.* (2013), which are derived from extensive full-wave simulations using the International Reference Ionosphere (IRI) plasma density profile. Related work using the same full-wave model has

been experimentally verified at  $\sim 20$  kHz using DEMETER satellite measurements of VLF transmitters (*Cohen et al.*, 2012). *Graf et al.* reports a set of curves in the same manner as Helliwell – power attenuation as a function of latitude, for two frequencies (2 kHz and 20 kHz), for dayside and nightside ionospheres. We then interpolate (or extrapolate) in log-space to find an attenuation factor for any latitude or frequency of interest ( $\approx 10^\circ - 70^\circ$ , and 200 Hz - 30 kHz).

We transition between the dayside and nightside attenuation curves using a Sigmoid function, with an approximate 1-hour transition width.

Figure 2.6 compares the *Graf et al.* (2013) and *Helliwell* (1965) attenuation curves, which model the integrated wave power losses between 65 km - 1500 km altitude as a function of frequency and geomagnetic latitude. Both models exhibit similar trends – higher attenuation towards the equator, and higher attenuation on the dayside – however the Helliwell curves report significantly greater attenuation overall. We can attribute this due to the electron density profile used in their calculation.

### 2.3.2 Models of the Ionosphere

In general, our treatment of wave propagation in the ionosphere is abstracted using the method described in section 2.3.1. However, in raytracing through the plasmasphere, we require a smoothly-varying transition between the plasmasphere and ionosphere models. Here we discuss two models of ionosphere electron density.

**IRI** The International Reference Ionosphere (IRI) is a standard model of several key plasma parameters – electron density, electron and ion temperatures, ion composition, and so forth. IRI provides detailed outputs as a function of location, altitude, and local time. The GCPM plasma model uses the IRI-2007 implementation (*Bilitza and Reinisch*, 2008); the simplified IRI model is derived from the IRI-2016 model (the most-current available version at time of writing).

**Simplified IRI** In order to both reduce our model parameter space, and to greatly decrease computation time, we pair a simplified version of IRI with a simplified version of GCPM. The IRI-2016 model was run for dayside and nightside ionospheres (12

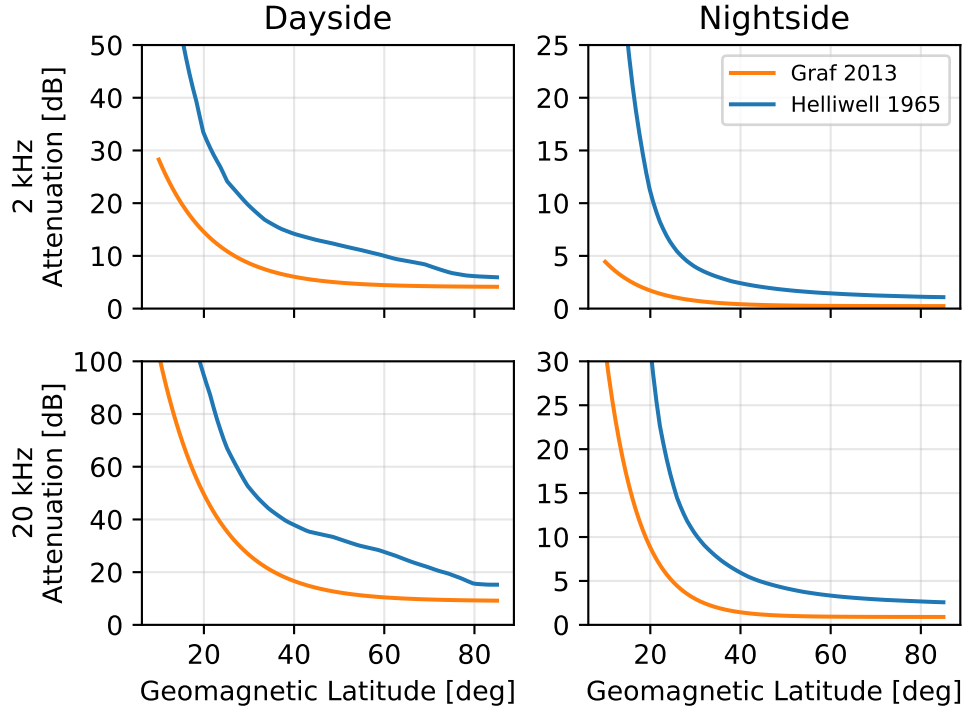


Figure 2.6: Trans-Ionosphere attenuation curves for the dayside and nightside, at 2 kHz and 20 kHz. Reproduced from *Graf et al. (2013)*, figure 7. The *Graf et al.* curves show markedly less attenuation than the previously-used *Helliwell* curves, especially at equatorial latitudes, and on the day side.

and 0 MLT), using all default settings, for January 1st, 2000. We then fit a multiple-Gaussian function to the electron density vs latitude, at an altitude of 1500 km, and at the  $F_2$  peak. Electron density variation with respect to altitude is approximated by a log-linear fit between 1500 km and the  $F_2$  peak. Finally, longitudinal variation is smoothed with a sigmoid function with a width of  $\sim 1$  hr. Figure 2.7 shows both the IRI electron density and the derived curve fits.

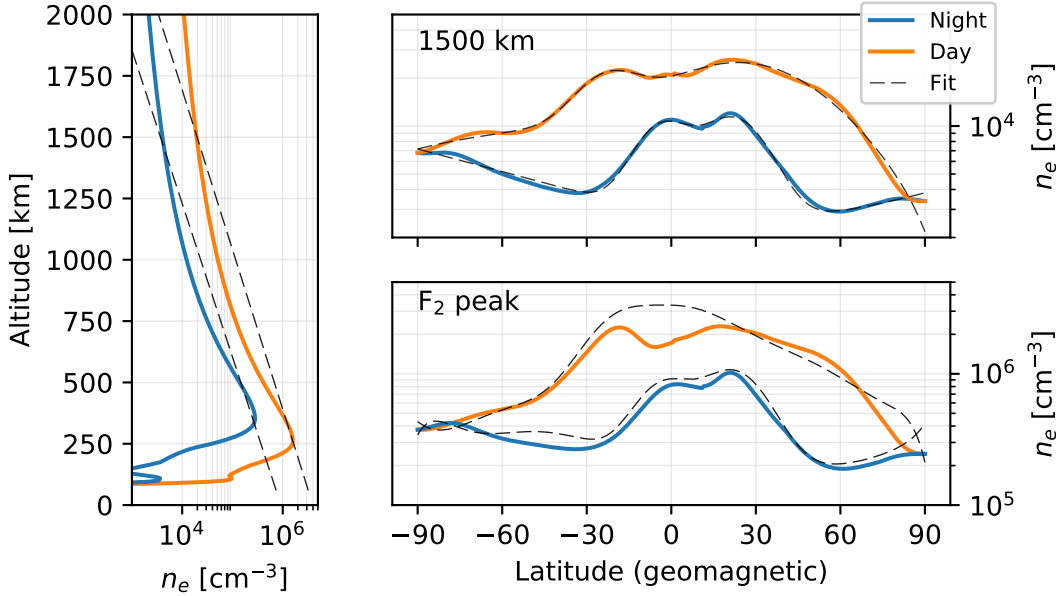


Figure 2.7: The IRI electron density model and derived curve fits. The left panel shows electron density variation as a function of altitude, for day and night. The right panels show electron density variation with respect to latitude, for (top) 1500 km and (bottom) the  $F_2$  peak (approx. 300 km). Dashed lines indicate the fitted curves used by the simplified IRI model.

## 2.4 The Earth's magnetic field

The Earth's magnetic field dictates the morphology and natural coordinate systems used in studying the near-Earth space environment. Here we discuss three models of the Earth's magnetic field, with increasing complexity and realism.

### 2.4.1 Models of the magnetic field

**Dipole** To first order, the Earth's magnetic field can be approximated as a dipole, with origin at the Earth's center, and a tilt of  $\approx 11^\circ$  from the axis of rotation. The dipole model, sometimes referred to as the “centered dipole” or “tilted dipole”, is reasonably accurate for midlatitude field measurements over the continental United

States, but can deviate significantly from the true field elsewhere. Similarly, the dipole field model is reasonably accurate for middle latitudes, below  $\approx 10$  Earth radii, but become increasingly inaccurate at higher latitudes, and at larger distances from the Earth, where the Earth's internal field is no longer dominant.

The dipole model, however, excels in its simplicity – the dipole magnetic field can be completely described in a closed form, and can be computed rapidly and reliably.

The dipole potential is given by:

$$\psi_{dip} = B_0 \left( \frac{R_e}{r} \right)^2 \cos \theta \quad (2.42)$$

The individual components of the magnetic field are given by the negative gradient of the scalar potential:

$$\mathbf{B} = -\nabla \psi \quad (2.43)$$

$$B_r = -2B_0 \left( \frac{R_e}{r} \right)^3 \cos \theta \quad (2.44)$$

$$B_\theta = -B_0 \left( \frac{R_e}{r} \right)^3 \sin \theta \quad (2.45)$$

$$B_\phi = 0 \quad (2.46)$$

Within this work we use  $B_0 = 31.5 \mu\text{T}$  and  $R_e = 6371 \text{ km}$ .

A single fieldline, determined by integrating the direction of the field vector, can be described by it's *L-shell* – the fieldline's altitude, in units of Earth radii, measured at the equator.

For the dipole field, the radius of a field line at any latitude is related by:

$$R(\lambda) = R_e L \cos^2 \lambda \quad (2.47)$$

The dipole field can then be used as an orthogonal coordinate system, with any location being specified by a latitude, longitude, and L-shell (McIlwain, 1961).

Within the plasmasphere, the dipole model works well. However, closer to the

Earth's surface the model becomes increasingly inaccurate, necessitating a higher-order model.

**IGRF** The International Geomagnetic Reference Field (IGRF) is a 13th-order spherical expansion model, with coefficients updated every few years based on terrestrial measurements (*Thébault et al.*, 2015). Within this work we use the IGRF-12 model as a realistic representation of the Earth's internal magnetic field.

IGRF is quick and simple to calculate at any given location, and is much closer to reality than a simple dipole field. However, due to the added complexity, there are not closed-form expressions for field line trajectories or L-shells, which can make dealing with IGRF (and any higher-order model) more cumbersome.

Figure 2.9 contrasts lines of constant L-shell between the dipole and IGRF models.

**Tsyganenko Corrections** The dipole and IGRF models represent the Earth's internally-generated magnetic field. However, as one moves further away from the Earth ( $L > \sim 8$ ), the Earth's internal field becomes less dominant, and external fields, namely forcing from the solar wind, cannot be ignored. The total field present in the space environment is the sum of both internal and external contributions.

Numerous models of the external field exist; within this work we consider the T05 external field model (*Tsyganenko and Sitnov*, 2005). The external field model exhibits seasonal and daily variation. However, for fieldlines below  $L \approx 6$ , the external field effects can be ignored.

Figure 2.8 contrasts the dipole, IGRF, and T05-corrected models in the meridional plane; Figure 2.9 illustrates the deviation in fieldline contours along the Earth's surface between the dipole and IGRF models.

## 2.5 The Plasmasphere

The plasmasphere is a region of the space environment surrounding the Earth, and a primary unknown within our modeling. The plasmasphere extends from an altitude of 1000km up to several Earth radii; typically it is divided into two separate regions:

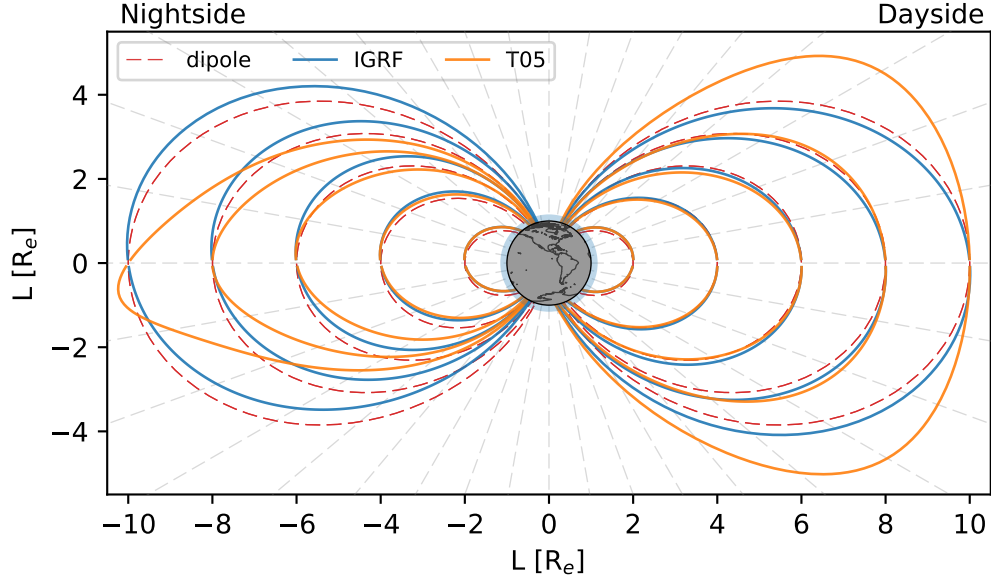


Figure 2.8: Three different magnetic field models, shown in the meridional plane, in geomagnetic coordinates: the tilted dipole, the IGRF model, and the Tsyganenko-Corrected IGRF model. Solar wind is incident on the right side.

a dense, relatively cold *inner plasmasphere*, and a sparse, relatively hot *outer plasmasphere* or *trough*. The transition boundary between the two regions is a sharp dropoff in plasma density called the *plasmapause*. The location of the plasmapause varies with magnetic local time (MLT) and solar activity conditions, but generally occurs between  $4 \pm L \pm 7$ . Forcing on the sun side tends to bring the location closer to the Earth. Figure 2.10 shows the modeled location of the plasmapause as a function of  $K_p$ , a measurement of space weather activity.

Much like the ionosphere, the plasmasphere is a highly variable region, depending on solar conditions ( $K_p$ ), location (latitude, longitude, field line), and time of day (MLT). The large spatial scales, high variability, and sparse availability of in-situ measurements require us to turn to empirical models of each region. We consider three primary models of electron and ion density.

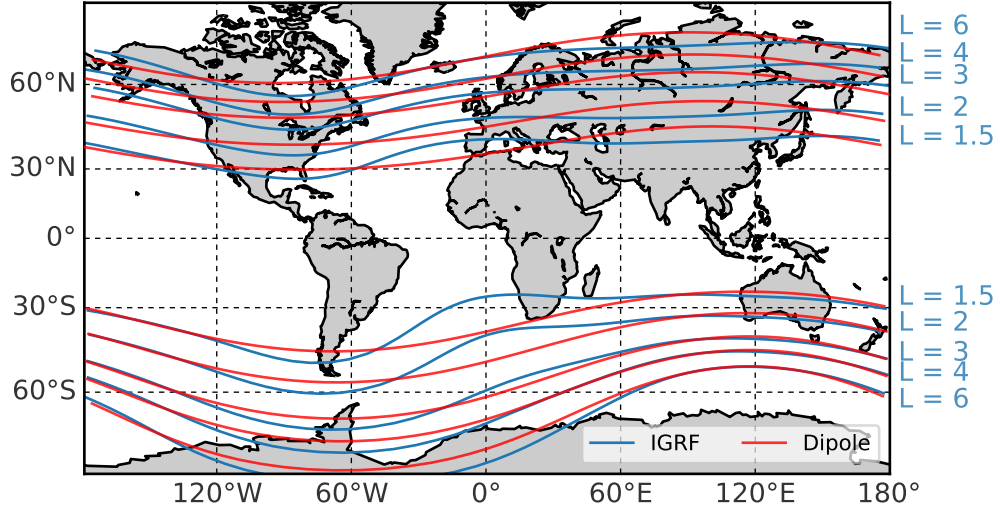


Figure 2.9: Fieldline contours along the Earth’s surface, shown for the dipole and IGRF models.

### Overview of Plasmasphere Density Models

**Ngo Model** The Ngo model is a legacy model used extensively in research at Stanford from the early 1980s through the mid-2000s, notably by *Lauben* (1998) and *Bortnik* (2005), and has heritage dating back to the early days of radioscientific research at Stanford (*Kimura*, 1966). The model uses a Diffusive Equilibrium (DE) (*Angerami*, 1963) model for the inner and outer plasmasphere, onto which the *Carpenter and Anderson* (1992) inner plasmasphere model is overlaid. This model was integrated into the legacy Stanford VLF raytracing code, and provided several adjustable parameters, including plasmapause location, constituent ratios, and the ability to include ducts.

**Global Core Plasmasphere Model (GCPM)** The Global Core Plasmasphere Model, initially developed in 2000 by *Gallagher et al.* (1999) with significant updates through the following decade, smoothly transitions between several regional models

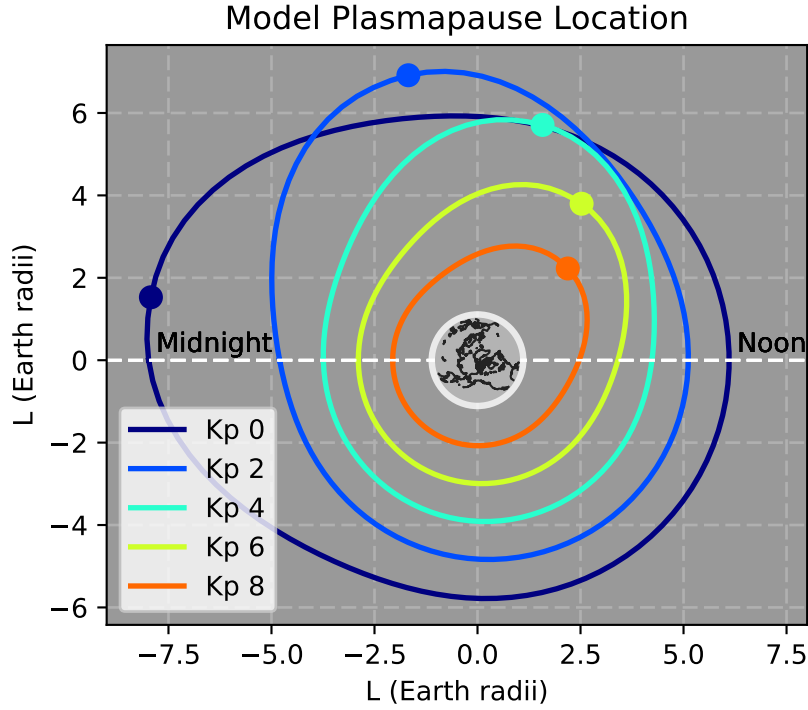


Figure 2.10: A model of the plasmapause location, as a function of  $K_p$  and magnetic local time. Taken from (*Gallagher et al.*, 1999)

to provide a continuous model of the plasmasphere. Within this work we use version 2.4, which was released in 2009 and made available by the Space Plasma Physics group at the NASA Marshall Space Flight Center (<https://plasmasphere.nasa.gov>). GCPM incorporates the *Carpenter and Anderson* (1992) inner plasmasphere model and the *Gallagher et al.* (1995) outer plasmasphere model, with an empirical fit of the plasmapause location between. The polar cap model is derived from *Persoon et al.* (1983) and *Chandler et al.* (1991). All models are connected smoothly to the IRI model of the ionosphere at lower altitudes. The combined GCPM model is parameterized by  $K_p$  and MLT.

**Simplified GCPM** GCPM aims to provide a dynamic, complete picture of the plasmasphere as a function of time and  $K_p$ ; however for our purposes GCPM provides

too much variation. Additionally, the combination and smoothing between many models is computationally slow. In order to provide quicker computation and to reduce the number of parameters to adjust, we have implemented a simplified version of GCPM.

This model uses the equatorial-plane GCPM model, including the plasmapause location. However we omit any variation in electron density along latitude, and assume densities are constant along each field line. As our region of interest lies primarily within low and mid latitudes, we omit the polar cap model altogether and simply merge the ionosphere into the equatorial trough model. Finally to simplify computation, we model the ionosphere using an empirical fit to IRI – one for noon, and one for midnight, with a smooth transition along longitude. Figure 2.11 shows a side-by-side comparison of the three models, for  $K_p = 2$ .

### 2.5.1 Ray Tracing

Whistler-mode waves in the magnetosphere propagate for very large distances, and with relatively little attenuation. Under certain conditions, these waves can persist from a few seconds to 1 or more minutes. Simulating the propagation of these waves using a full-wave method would be extremely intractable with current computational resources. However we can use ray tracing to approximate their behavior.

Ray tracing is a technique from geometric optics which tracks the position and velocity of a coherent wave packet – essentially, approximate the behavior of a wave packet to that of a photon, and evaluate the packet’s velocity and wavenormal vector with respect to time. Ray tracing is best suited for coherent, monochromatic wave packets, with no attenuation, dispersion, or mode coupling.

Ray tracing was first applied to the whistler mode by *Haselgrave* (1954) using a graphical technique, then subsequently by *Haselgrave and Haselgrave* (1960) and *Kimura* (1966) for numerical computation. These papers worked in curvilinear coordinates with respect to a magnetic field line. Haselgrave’s Equations have been used extensively by numerous magnetospheric scientists (*Kimura*, 1966; *Edgar*, 1972; *Ngo*, 1989; *Jasna*, 1993; *Lauben*, 1998; *B.Peter*, 2007; *Bortnik*, 2005; *Kulkarni*, 2009),

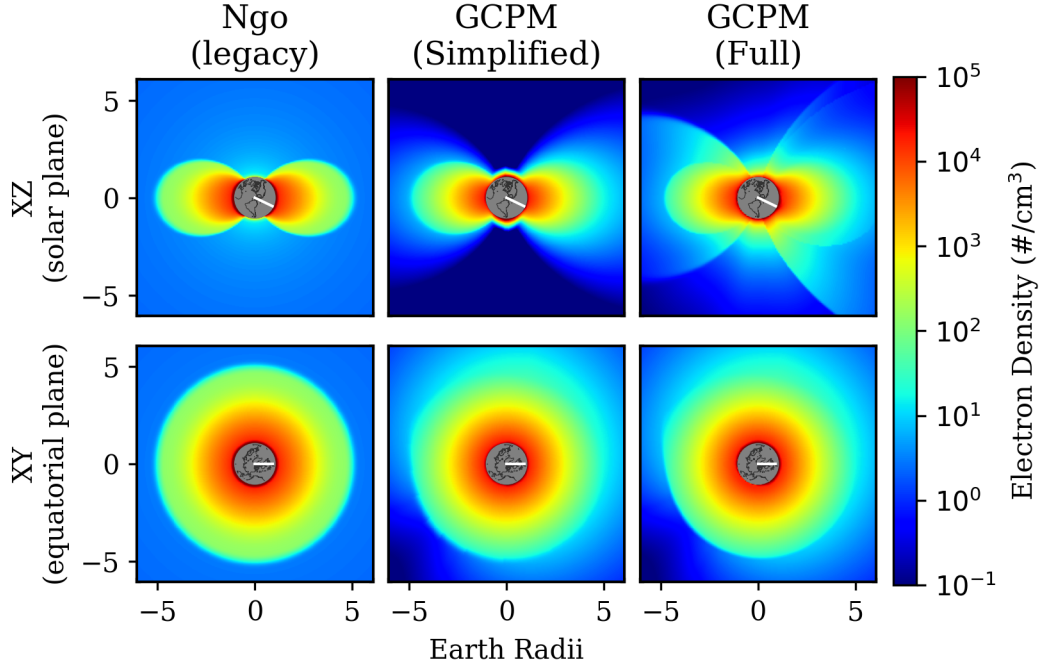


Figure 2.11: A comparison of three plasmasphere models: Ngo, simplified GCPM, and full GCPM, for a relatively quiet plasmasphere ( $K_p = 2$ ). The top row shows electron density in-plane with the direction of solar influx; the bottom row shows a top down (equatorial cross-section) view. The white line indicates the solar axis. Only electron density is shown, as additional plasma constituents are derived from electron density.

several using the so-called “Stanford Ray Tracing Program” – a legacy Fortran code which evaluated the Haselgrove equations in two dimensions. Our work uses a slightly different code originally developed by Dr. Forrest Foust (*Golden et al.*, 2010), and is designed for flexibility with respect to plasma density and magnetic field models. Rather than work in curvilinear coordinates with explicit derivatives, we adopt a more-general formulation, using a three-dimensional Cartesian frame and numerically-evaluated derivatives.

We begin with the fundamental ray-tracing equations, as given by *Haselgrove and Haselgrove (1960); Stix (1992)*:

$$\frac{d\mathbf{r}}{dt} = \frac{\nabla_k F}{\partial F / \partial \omega} \quad (2.48)$$

$$\frac{d\mathbf{k}}{dt} = \frac{\nabla_r F}{\partial F / \partial \omega} \quad (2.49)$$

$$(2.50)$$

Constrained such that:

$$F = F(\mathbf{r}, t, \mathbf{k}, \omega) = 0 \quad (2.51)$$

Equation 2.48 is simply  $\frac{\nabla_k F}{\partial F / \partial \omega} \approx \frac{\partial F / \partial k}{\partial F / \partial \omega} = \frac{\partial \omega}{\partial k} = v_g$ , the group velocity of a wave packet. The corresponding equation describing the evolution of the wavenormal vector (2.49) is less intuitive, although an analogy can be drawn to Hamiltonian mechanics, in which  $\omega$  represents a velocity, and  $k$  a momentum.

The function  $F$ , our “conserved quantity”, is simply the cold plasma dispersion relation given by equation 2.30.

The raytracing equations are a set of coupled, first-order differential equations; solutions to which require some subtlety, but can be addressed using standard numerical techniques.

First, note that we can solve the set at a given time, then evolve the system forward some finite time step. However, the constraint  $F = 0$  may not be strictly held afterward. We assert that the error in this constraint must be small; which in turn implies that the background medium must be smoothly-varying – i.e., changing on a spatial scale much greater than our forward step, and of the wavelength of interest. This assumption is known as the *WKB Approximation*.

### Adaptive Timestepping

The process of raytracing, then, is to 1) solve the dispersion relation (2.30) to find the refractive index; 2) compute the velocity vector and step the system forward in time; and 3) re-evaluate at the new position to assure that the condition  $F=0$  is satisfied. However, properly selecting the timestep is of critical importance – too large a timestep and positional errors will accumulate, or the ray will slip out of a

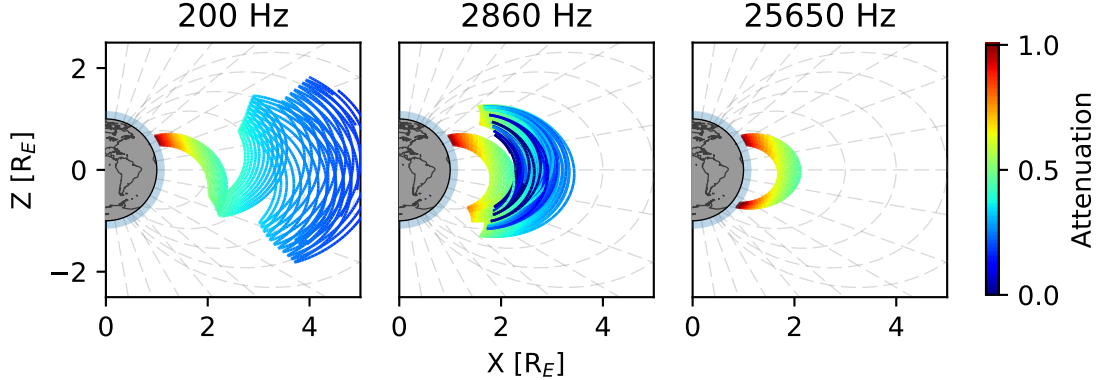


Figure 2.12: Example ray families as computed by the raytracer

propagating mode; too small and computational speed and memory usage suffers. We use an adaptive *Runge-Kutta-Fehlberg* (RK45) (*Fehlberg*, 1969; *Mathews and Fink*, 2004) method to continuously update the timestep as the raytracer progresses. RK45 is a common technique for solving ordinary differential equations.

The RK45 method approximates a solution with an initial stepsize  $dt$  using two spline fits: a fourth-order and a fifth-order. The error in the step is taken to be the difference between the two estimates. If the error is above a specified tolerance  $\epsilon$ , the stepsize is reduced and the evaluation is repeated. Additionally, if the error is below a specified tolerance ( $\epsilon/10$  in our implementation), the stepsize is increased. The result is a variable time axis with finer resolution in regions of high variability, while enabling longer timesteps in smooth regions for computational efficiency. See appendix B for a detailed description of the Runge-Kutta method.

### 2.5.2 Landau Damping

The cold-plasma formulation of raytracing described above evaluates the trajectory and wavenormal angle of a wave packet. However, it assumes zero attenuation of wave energy. While it is possible to account for wave attenuation in ray tracing using warm plasma corrections (*Sazhin*, 1993; *Heney*, 1980), we follow the same approximation as used in the legacy ray tracing code, and calculate attenuation along the cold-plasma

raypath according to Landau damping.

Landau damping, originating in a seminal work by *Landau* (1946), is a resonant interaction between a wave and the distribution of electrons and ions comprising the background medium. The Landau mechanism is an interaction with parallel streaming particles and the wave's electric field. Resonant particles are accelerated or decelerated by the wave's electric field; if a majority of the resonant electrons have velocities slightly below that of the wave, then a coherent effect exists, the wavefront imparts some net energy to the plasma, and the wave is attenuated. Conversely, if the majority of resonant particles are moving faster than the wave, some of their energy can be imparted to the wavefront, inducing *wave growth* (*Chen*, 1983; *Kulkarni*, 2009).

Landau damping can have multiple resonances (in which the particle has multiple complete rotations per rotation of the wave). The lowest resonant mode is known as the *Landau* resonance, while the  $\pm 1$  modes are referred to as the *Cyclotron* resonances. Higher-order modes remain nameless.

We use the expressions for Landau damping as formulated by *Brinca* (1972). *Brinca* derived expressions for Landau damping assuming a cold background plasma with a sparse warm distribution added, for Whistler waves propagating at an arbitrary angle to the background magnetic field. Inputs to this formulation are the familiar Stix parameters (equations 2.26 - 2.27), which are in turn a function only of location and wave frequency; the wavenormal angle with respect to the background magnetic field; and a distribution function which specifies the energies (and thus velocities) of thermal electrons. The full set of Landau damping equations is given in appendix A.1.

Interestingly, *Brinca*'s work was motivated by measurements of whistler-mode wave growth, rather than attenuation. Our implementation follows suit, and is equally capable of returning growth or damping, depending on the plasma model used. However, throughout this research, wave growth has been exceedingly rare.

### Thermal electron distributions

The extent to which a wave is amplified or damped is heavily dependent on the energy distribution of background electrons. The energy distribution, or temperature profile, is specified as a normalized function in phase space – a function of position and velocity, which is normalized to 1:

$$f = f(\mathbf{r}, \mathbf{v}, t) \quad (2.52)$$

$$= f(\mathbf{r}, v_{\perp}, v_{\parallel}, t) \quad (2.53)$$

$$\int_0^{\infty} f dv_{\perp} = 1 \quad (2.54)$$

$$(2.55)$$

Two distribution functions are used in similar work – the *Bell* (2002) distribution, which was derived from POLAR spacecraft measurements of the inner plasmasphere, and the *Bortnik et al.* (2007) distribution, which is based on CRRES spacecraft measurements above  $L \approx 7$ .

We use the phase space density function as described in *Golden et al.* (2010), which smoothly transitions between the *Bell* (2002) model inside the plasmapause, and the *Bortnik et al.* (2007) model outside the plasmapause. Figure 2.13 shows an example of the distribution function.

## 2.6 The Radiation Belts

The term “Radiation Belts” or “Van Allen belts” refer to the trapped distributions of sparse, very-high-energy electrons, which exhibit two shell-like enhancements which comprise the inner and outer radiation belts. First measured in 1958 by Geiger counters aboard satellites 1958 $\alpha$  and 1958 $\gamma$  of the Explorer program, the radiation belts were one of the earliest discoveries of the American space program (*Van Allen*, 1958). The vast majority of plasmasphere electrons are “cold”, and have kinetic energies well under  $\sim 1$  eV. However, radiation belt electrons, while sparse in density,

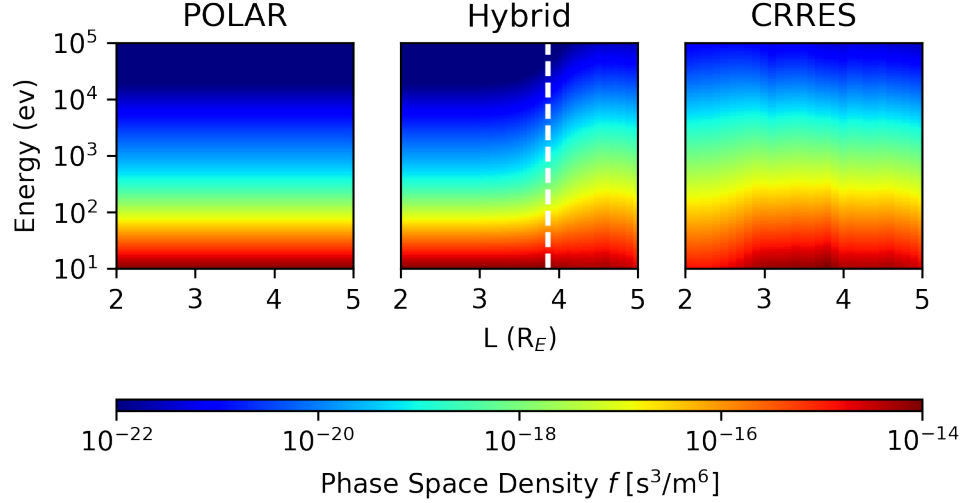


Figure 2.13: Example phase-space density functions, shown for  $A_e=1.6$ ,  $K_p=4$ ,  $\alpha=45^\circ$ , and  $MLT=18$ . The POLAR model is used inside the plasmapause, and the CRRES model outside the plasmapause. The hybrid model smoothly transitions between the two. The plasmapause, at  $L \approx 4$ , is marked by the dashed white line.

can be highly relativistic, with energies approaching 10 MeV.

Section 2.5 describes the density of electrons and ions in the near-Earth environment. Absent from these models, however, is a discussion of electron and ion energies. The model in section 2.5.2 assigns an energy distribution to electrons in the  $\sim 1$  eV range to model a warm plasma; the higher energies of radiation belt electrons, however, necessitate a different model.

We model the trapped electron population using the AE8 density model (Vette, 1991). AE8 provides omnidirectional, integral fluxes of high-energy electrons as a function of L-shell energy. AE8 is the culmination of several decades of radiation belt studies by the National Space Science Data Center (NSSDC), with the first efforts originating with Vette (1966). AE8 combines measurements from  $\sim 94$  different instruments across  $\sim 24$  satellite missions from the 1960s and 1970s, which spanned a wide range of orbits, from LEO out to geostationary (Cayton, 2005).

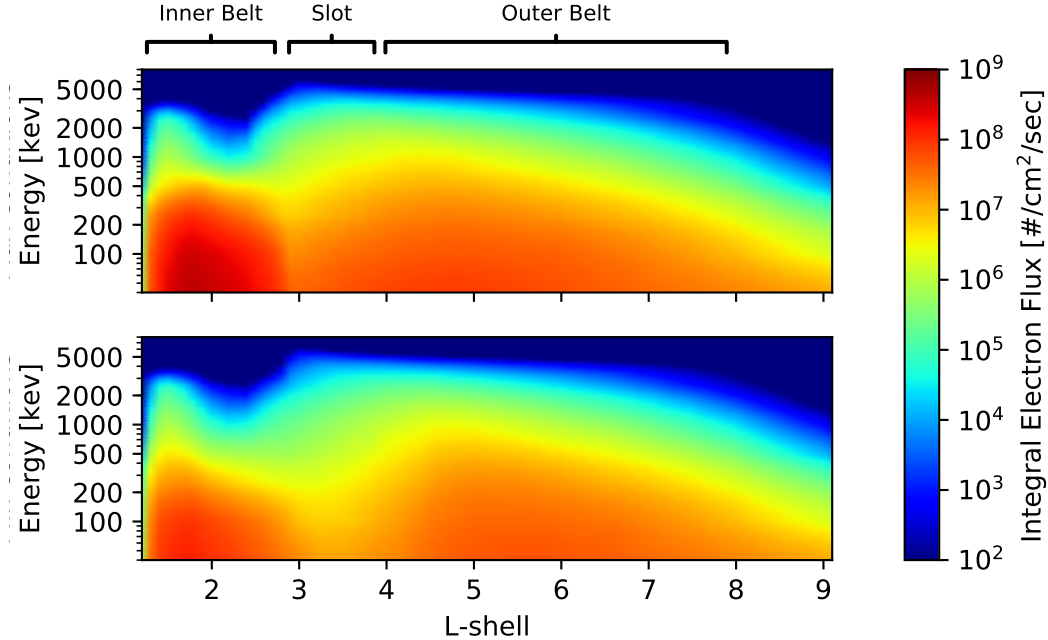


Figure 2.14: Integral flux for energetic electrons in the radiation belts, as reported by the AE8 model (*Vette*, 1991). The top frame shows the model of maximum conditions, and the bottom frame minimum conditions. The two radiation belts are visible as enhancements within  $L \approx 2 - 3$  for the inner belt, and  $L \approx 4 - 7$  for the outer belt. The belts are separated by a depletion known as the “slot” region.

Figure 2.14 shows the AE8 model output for minimally-populated and maximally-populated conditions.

The AE8 model reports omnidirectional, integral fluxes – that is, the total electron flux integrated over a spherical surface – at the geomagnetic equator. However we require finer detail in directional flux of electrons, which we model via a distribution of pitch angles. *Lauben* (1998) assumed the simplest distribution, with electrons uniformly-distributed in pitch angle up to the loss cone. *Bortnik* (2005) compared the square distribution to a more-realistic, sinusoidal distribution. Here we assume a sinusoidal pitch-angle distribution along with the AE8 flux density model. Figure 2.15 contrasts the square and sinusoidal distribution functions.

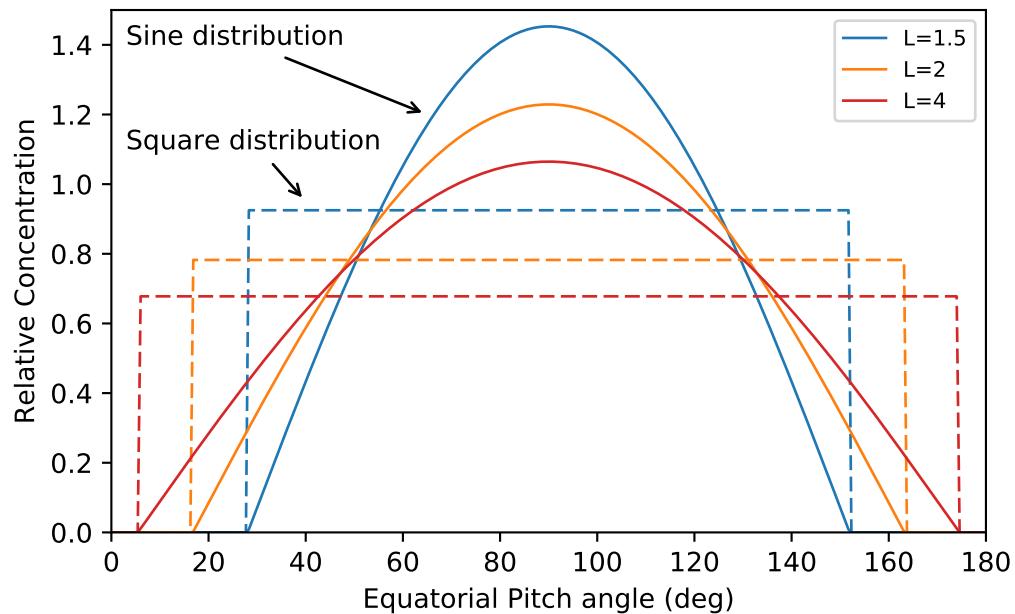


Figure 2.15: Two models of the distribution in pitch angle of radiation belt electrons. The simplest model is a square-shaped distribution, wherein pitch-angles are equally represented within the trapped population. A more realistic model is a sinusoidal distribution. Densities within the loss cone ( $\alpha < \alpha_{lc}$ ) are assumed to be zero.

## 2.7 Wave-Particle Interactions

A trapped particle follows a fixed trajectory, bouncing indefinitely back and forth between its reflection points at the northern and southern hemispheres. The particle's local pitch angle varies with latitude; however in the absence of external interactions, the pitch angle remains the same at each pass. For convenience, we can relate any local pitch angle back to the equatorial pitch angle through conservation of the first adiabatic invariant (2.4).

$$\sin^2 \alpha(\lambda) = \frac{B(\lambda)}{B_{eq}} \sin^2 \alpha_{eq} \quad (2.56)$$

A trapped particle's equatorial pitch angle remains a constant of the motion. However, it can be altered by means of a perturbation to the local magnetic field. Generally, small perturbations will be incoherent, and have negligible net effect on a particle's trajectory when compared to the background magnetic field. In the case of resonant wave-particle interactions, the particle's gyrorotation and the wave's magnetic field can be coherent, and have a significant effect on the particle's trajectory.

An essential characteristic of resonant wave-particle interactions is that while some energy can be imparted through the wave's electric field, no energy is exchanged through the magnetic field – rather, the perturbative effect of the wave magnetic field primarily shifts the particle's own kinetic energy between the parallel and perpendicular modes ( $v_{\parallel}$ ,  $v_{\perp}$ ).

### 2.7.1 Resonant Interactions

We begin by considering the resonant interaction between a monochromatic, elliptically-polarized wave, propagating obliquely (i.e., not strictly aligned with the background magnetic field). We can then calculate the resonant, doppler-shifted perturbative fields  $\mathbf{E}_w$ ,  $\mathbf{B}_w$ , and calculate the change to a test particle's momentum using the relativistic Lorentz force. This analysis stems from *Bell* (1984), and has been used in numerous successive studies – *Jasna* (1993); *Lauben* (1998); *Bortnik* (2005), and others.

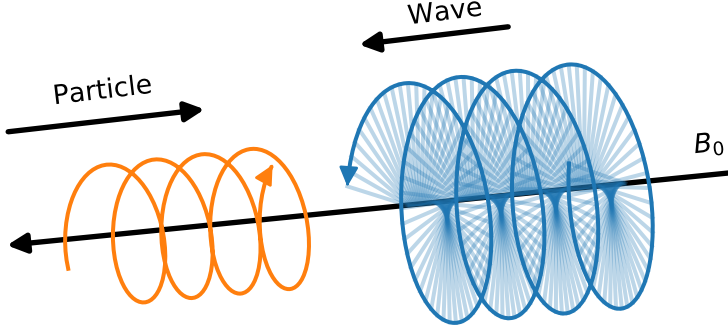


Figure 2.16: An illustration of a counter-streaming wave-particle interaction. At resonance, a gyrorotating particle sees an effective constant electric and magnetic field. Resonant interactions can occur in co-streaming (same direction) or counter-streaming (opposite direction) encounters.

The condition for resonance is given by *Chang and Inan* (1983):

$$\frac{d\eta}{dt} = \omega + v_z^{res} k_z - m\omega_c/\gamma \approx 0 \quad (2.57)$$

where  $\eta$  is the angle between the right-hand circular component of the wave magnetic field ( $B_r$ ) and the resonant particle's perpendicular velocity vector ( $v_\perp$ ),  $\omega$  is the wave frequency,  $m \in \mathbb{Z}$  is the resonance order, and  $\gamma = (1 - (v^{res}/c)^2)^{-1/2}$  is the relativistic correction factor.

We use the *Bell* (1984) expression for change in pitch angle with respect to time, corrected for relativistic factors by *Jasna* (1993); *Bortnik et al.* (2006):

$$\frac{d\alpha}{dt} = \frac{m_e \omega_{rm}^2}{k_z p_\perp} \left( 1 + \frac{\cos^2 \alpha}{m \omega_c / \omega - 1} \right) \sin \eta + \frac{1}{m_e \gamma} \frac{p_\perp}{2 \omega_c} \frac{\partial \omega_c}{\partial z} \quad (2.58)$$

with the following parameter definitions:

$$\beta = \frac{k_x p_\perp}{m_e \gamma \omega_c} \quad (2.59)$$

$$k_z = k \cos \theta = (\omega \mu / c) \cos \theta; \quad k_x = k \sin \theta \quad (2.60)$$

$$\omega_{\tau m}^2 = (-1)^{m-1} \omega_{\tau 0}^2 [J_{m-1}(\beta) - \alpha_1 J_{m+1}(\beta) + \gamma \alpha_2 J_m(\beta)] \quad (2.61)$$

$$\omega_{\tau 0} = \frac{\omega_1 k_z p_\perp}{\gamma m_e} \quad (2.62)$$

$$\omega_1 = \frac{e}{2m_e} (B_x^w + B_y^w); \quad \omega_2 = \frac{e}{2m_e} (B_x^w - B_y^w) \quad (2.63)$$

$$\alpha_1 = \frac{\omega_2}{\omega_1} \quad (2.64)$$

$$\alpha_2 = \frac{e E_z^w}{\omega_1 p_\perp} \quad (2.65)$$

$$R_1 = \frac{E_x^w + E_y^w}{B_x^w + B_y^w}; \quad R_2 = \frac{E_x^w - E_y^w}{B_x^w - B_y^w} \quad (2.66)$$

where  $e$  and  $m_e$  are the electron charge and rest mass,  $p_\perp$  is the perpendicular component of the particle's momentum,  $J_i$  are Bessel functions of the first kind, and  $E_{x,y,z}^w$ ,  $B_{x,y,z}^w$  are the vector components of the incident wave, oriented such that the z-component is parallel to the background magnetic field.

A full derivation of equations (2.58) - (2.66) is beyond the scope of this dissertation; however the full derivation is explained in the theses of *Bortnik* (2005), *Jasna* (1993), and *Bell* (1984).

While the full set of equations (2.58) - (2.66) is complex, we can identify several broad trends: First,  $\partial \alpha / \partial t \propto \sin \eta$ , which implies that, when the resonance condition is not met, oscillating changes will have no cumulative effect. Second,  $\partial \alpha / \partial t \propto \alpha$ , which increases the complexity of the solution space; however we can introduce a simplification by assuming that changes in pitch-angle are small, and therefore only particles with pitch angles very near the loss cone will be of significance. We can therefore introduce a relationship between pitch angle and  $v_\perp$  and  $p_\perp$  (*Bortnik et al.*, 2006):

$$v_z^{res} = \frac{\pm \sqrt{\omega^2 k_z^2 + [(m\omega_c)^2 - \omega^2][k_z^2 + (\frac{m\omega_c}{c \cos \alpha_{lc}})^2] - \omega k_z}}{k_z^2 + (\frac{m\omega_c}{c \cos \alpha_{lc}})^2} \quad (2.67)$$

## 2.7.2 Recovering Wave Amplitudes from Poynting Flux

Required in our modeling is the ability to link the results of raytracing to the wave-particle interaction model. However, raytracing tracks only coarse-grained wave parameters – wavenormal vector, propagation angle with respect to the background magnetic field, and the background plasma parameters. We use the formulation from *Bell* (1984), which has since been used by *Jasna* (1993); *Lauben* (1998); *Bortnik et al.* (2006), to relate the Poynting flux and the individual wave components  $B_x^w, B_y^w, B_z^w$ .

Starting from the definition of Poynting flux  $\mathbf{S}^w = (1/2)\text{Re}(\mathbf{E}^w \times \mathbf{H}^w)$ , *Bell* (1984) finds a relation to a single magnetic field component,  $B_y^w$ :

$$\|B_y^w\| = \frac{2\mu_0\rho_2^2 X^2 \eta \cos \theta \|\mathbf{S}^w\|}{c\sqrt{(\tan \theta - \rho_1\rho_2 X)^2 + (1 + \rho_2^2 X)^2}} \quad (2.68)$$

$$X = \frac{P}{P - \eta^2 \sin^2 \theta} \quad (2.69)$$

$$\rho_1 = \frac{E_z^w}{E_y^w} = \frac{(\eta^2 - S)\eta^2 \sin \theta \cos \theta}{D(\eta^2 \sin^2 \theta - P)} \quad \rho_2 = \frac{E_x^w}{E_y^w} = \frac{\eta^2 - S}{D} \quad (2.70)$$

where  $\rho_1, \rho_2$  are the wave polarization ratios,  $\eta$  is the wave refractive index,  $\theta$  is the angle between the wavenormal and the background magnetic field,  $\mathbf{S}^w$  is the Poynting flux, and  $S, D$ , and  $P$  are the Stix parameters defined in (2.26) and (2.27).

The remaining five wave components are given by:

$$E_x^w = \frac{\|cB_y^w(P - \eta_x^2)\|}{P\eta_z} \quad (2.71)$$

$$E_y^w = \frac{\|E_x^w D\|}{S - \eta^2} \quad (2.72)$$

$$E_z^w = \frac{\|E_x^w \eta_x \eta_z\|}{\eta_x^2 - P} \quad (2.73)$$

$$B_x^w = \frac{\|E_x^w D \eta_z\|}{c(S - \eta^2)} \quad (2.74)$$

$$B_z^w = \frac{\|E_x^w D \eta_x\|}{c(X - \eta^2)} \quad (2.75)$$

## 2.8 The GLD360 Lightning Dataset

One could not study the global impact of LEP without a measurement of global lightning activity. Lightning is a persistent phenomenon, with an average of  $\sim 100$  strokes per second globally at any given time of day or year (*Brooks, 1925; Orville and Spencer, 1979*).

Two primary techniques are used in the measurement of lightning distributions – optical / infrared detection from space, and geolocation techniques using surface measurements of the guided VLF emissions, or '*spherics*', which propagate in a waveguide-like manner between the Earth and the Ionosphere.

Early optical data measurements were performed in the 1970s by the U.S. Air Force, using the Defense Meteorological Satellite Program (DMSP) satellites, which served to reveal the global distribution of lightning – generally over land masses, and towards the equator. However, space-based optical techniques are limited to nighttime measurements, do not operate in real time, and must be performed amidst other parasitic light sources (*Orville, 1995*).

Surface-based radio detection of lightning has been in use as early as the 1920s, by magnetic direction finding (MDF) using crossed loop antennas (*Horner, 1954, 1957*). Such detection methods were primarily used for weather measurements before the advent of weather radar, and have seen use in early detection of forest fires

(*Krider et al.*, 1980). Terrestrial measurements have an advantage in that they can operate during both daytime and nighttime, and have detection ranges on the order of hundreds of kilometers, due to the guided propagation of 'spherics.

Large-scale detection networks became available in the early 1990s, with the U.S. National Lightning Detection Network (NLDN). NLDN provides near-real-time measurements of lightning across the continental United States using a distributed array of 114 sensors in the VLF / LF (400 Hz - 400 kHz) range. NLDN reports cloud-to-ground detection efficiencies on the order of  $\sim 90\%$  (*Nag et al.*, 2011).

Within the last decade, advances in processing techniques have fostered the ability to perform global lightning detection with a distributed array of sensors. We use the Global Lightning Dataset (GLD360), which uses a combination of time-of-arrival and direction-finding techniques, along with a precomputed waveform bank, to achieve global cloud-to-ground detection ratios on the order of  $\sim 60\%$  (*Said et al.*, 2010). GLD360 is a commercial service operated by *Vaisala, inc.*.

GLD360 parameterizes cloud-to-ground lightning discharges by their location (latitude, longitude), and their peak current,  $I_0$ , as given in section 2.2. Figure 2.17 shows the annual flash rate density reported by GLD360 over a two-year period between August 2014 and April 2016; figure 2.18 shows the average squared current density (from equation (2.37),  $S \propto I_0^2$ ). Within this work we take the GLD360 dataset to be the ground truth measurement of global lightning activity.

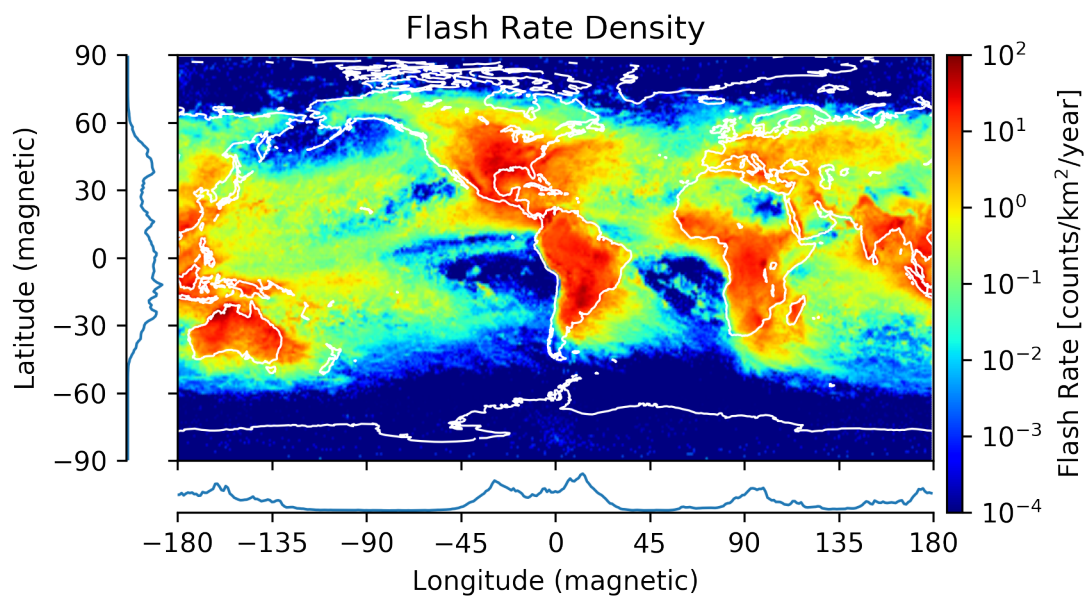


Figure 2.17: The average global flash rate distribution, as measured by the GLD360 sensor network, taken over a period between August 2014 and April 2016. The side plots show the relative density vs latitude and longitude.

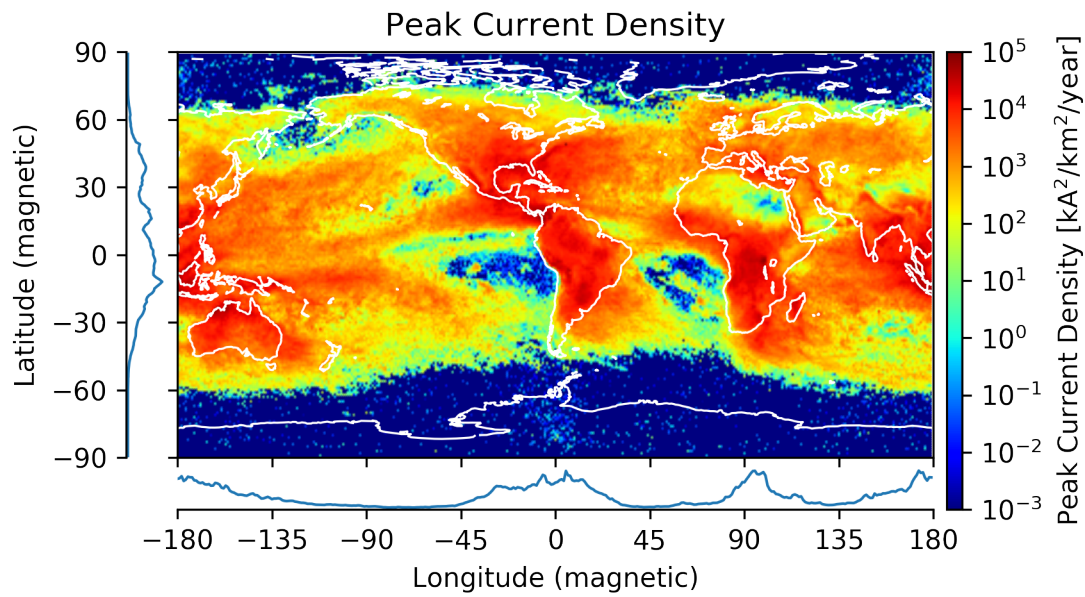


Figure 2.18: The average global peak current distribution, as measured by the GLD360 sensor network, taken over a period between August 2014 and April 2016. The side plots show the relative density vs latitude and longitude. While the morphology is similar to figure 2.17, scaling by the average peak current indicates a possible increase in energy over the oceans.

# Chapter 3

## VLF energy in the Near-Earth Environment

The purpose of this chapter is to provide a quantifiable assessment of the persistent radio wave energy in the near-Earth space environment due to lightning-generated whistlers. The morphology of LEP (time evolution, spatial extent at the Earth’s surface, and so forth) are primarily determined by the location of wave-particle interactions; additionally, wave-particle interactions with whistlers are hypothesized to be the primary cause of slot-region electron depletions, and the “impenetrable barrier” below  $L \sim 2$ .

Lightning-generated whistlers are sporadic, and exist alongside a multitude of radio wave activity, such as VLF chorus and plasmaspheric hiss, making a correlated *in-situ* measurement challenging. Within this chapter we simulate the relative VLF energy ( $L$ -shell, latitude, longitude) in the near-Earth space environment, in volumetric units [ $J/m^3$ ], as a means of assessing their relative contribution to the persistent radio spectrum.

### 3.1 Methodology

Our simulation is divided into two portions: First, a simulation of persistent VLF energy due to a single flash originating at a fixed latitude, and second, an integration

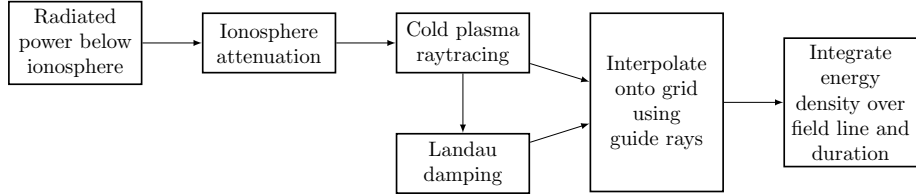


Figure 3.1: Block diagram of the average energy density calculation for a single flash.

over a measured lightning dataset, using scaled and shifted “stencils” for each flash.

## 3.2 Persistent Energy from a Single Flash

Figure 3.1 shows the steps required to compute the average energy imparted from a single lightning discharge. The resulting stencil has dimensions of L-shell and longitude.

1. First we model the sub-ionosphere power spectrum generated from a flash with a known peak current, using the methodology of section 2.2.
2. We then propagate the energies through the ionosphere, using the attenuating slab approximation method of section 2.3.1.
3. We map the time-integrated effective power above the ionosphere ( $J/m^2$  at 1000 km altitude) to an energy density along a fixed grid using a set of pre-computed “guide rays” using the methodology in section 2.5, the Landau damping from section 2.5.2, and the novel interpolation scheme described below.
4. In order to account for multiple crossings at each grid point, and to reduce our output space across different latitudes, we store the time-averaged energy density along each field line.

### 3.2.1 Radiated power above the ionosphere

Figure 3.3 shows the illumination below the ionosphere resulting from a single 100 kA discharge, as a function of frequency and radial distance. The illumination pattern

Table 3.1: Simulation Parameters

Ray Tracing Parameters:	
Plasmasphere model	Simplified GCPM
Magnetic field model	Dipole
Maximum error tolerance	$1 \times 10^{-3}$
Maximum timestep	5 ms
MLT	0 and 12
$K_p$	{0, 2, 4, 6, 8}
Latitude spacing	1°
Longitude spacing	1°
Frequency range	200 Hz - 30 kHz
Coarse Frequencies	33 (log-spaced)
Grid and Interpolation Parameters:	
Fine-scale Frequencies	50
Output L-shell range	1.2 - 8
Output L-shell spacing	0.05
Output latitude spacing	1°

given in equation (2.38) is independent of location along the Earth's surface. We multiply this illumination pattern by the absorption model in section 2.3.1 to determine illumination above the ionosphere. Figure 3.3 shows example illumination patterns for a set of flash latitudes and MLT.

By integrating over latitude, longitude, and frequency, we can estimate the total energy imparted to the magnetosphere by a flash at a given latitude, for daytime and nighttime conditions, as shown in figure 3.4. Our illumination model scales with peak current squared; when combined with the updated ionosphere attenuation curves from 2.6, we see significant overlap between day and night. A strong, midlatitude flash on the day side can easily impart similar energy as a less-intense or lower-latitude flash on the nightside.

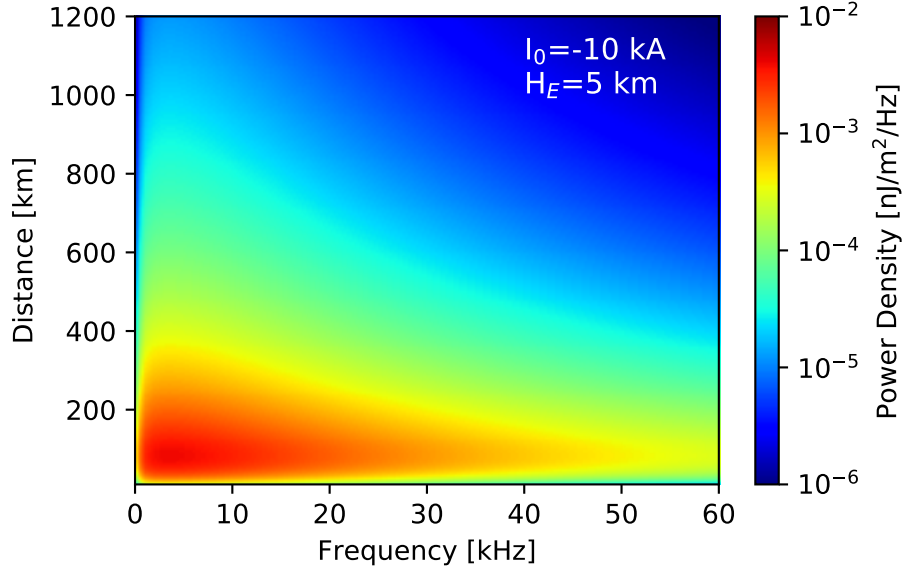


Figure 3.2: Vertically-propagating power density below the ionosphere from a single 100kA cloud-to-ground discharge with  $H_E = 5 \text{ km}$ , as a function of frequency and radial distance. Adapted from *Marshall et al.* (2011).

### 3.2.2 Gridding and Interpolation

We now have a model of the total energy above the ionosphere, at an altitude of 1000 km, divided into gridded bins in latitude, longitude, and frequency. The next step required is to map the energy within each cell out into the plasmasphere. We accomplish this task using a “guide ray” formulation, as illustrated in figure 3.5.

Using the ray tracing and Landau damping technique from section 2.5, we compute rays in  $1^\circ$  steps in both latitude and longitude, within 1000 km of the incident flash, for 33 logarithmically-spaced frequencies between 200 Hz and 30 kHz. Rays are computed for 20 seconds. See table 3.1 for a list of various parameters used. In order to generalize across all longitudes, we use the dipole magnetic field model and the simplified GCPM plasmasphere model. Additionally, we restrict raytracing deviation to the meridional plane to omit any numerical instabilities introduced. The computed rays are then interpolated onto a uniform time axis using one-dimensional linear

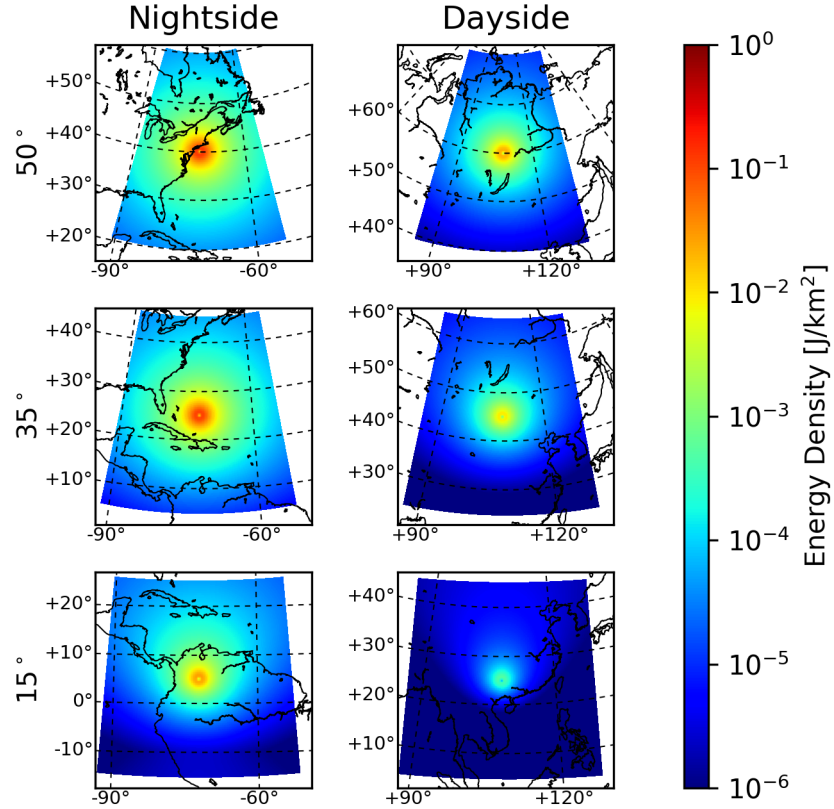


Figure 3.3: Illumination pattern, integrated over frequency, after ionospheric attenuation (altitude = 1000 km). The ionosphere imparts stronger attenuation at equatorial latitudes, and on the dayside. The pre-ionosphere illumination pattern is toroidal, with a central null directly over the incident flash.

interpolation for each parameter.

We make the assumption that the energy bounded by the set of 8 guide rays (two latitudes, two longitudes, two frequencies) remains bounded by these rays as they propagate. Furthermore, we assume that our interpolated timesteps are much larger than the envelope of the wave packet (see figure 2.5). Therefore, the initial energy within each cell is bounded by a four-dimensional voxel, determined by two adjacent timesteps  $t_{n-1}, t_n$  of the guide ray set  $\{(lat_1, lat_2), (lon_1, lon_2), (f_1, f_2)\}$ .

Next, we map the energy within each voxel to our output grid coordinates – chosen

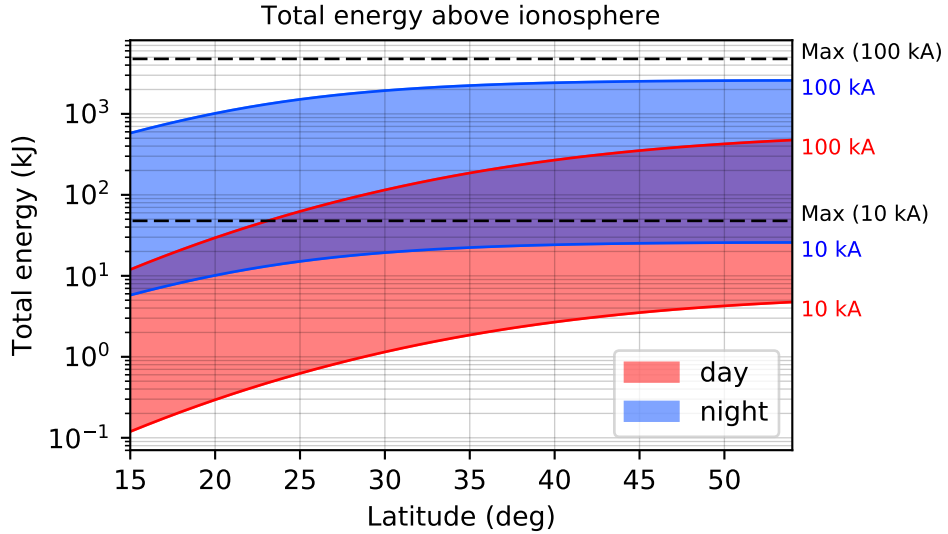


Figure 3.4: Integrated energy above the ionosphere from a single discharge, as a function of geomagnetic latitude. Energy scales quadratically with peak current; totals for 10 kA (an average flash), and 100 kA (a strong, but not unreasonable flash) are overlaid. The dashed lines indicate the total energy released below the ionosphere, before attenuation –  $\approx 50$  kJ for 10 kA, and  $\approx 4$  MJ for 100 kA.

here to be  $1^\circ$  steps in latitude,  $0.25^\circ$  in longitude, and  $0.05$  L-shell. We accomplish this task using an n-dimensional Delaunay triangulation construction (*Delaunay*, 1934; *Lee and Schachter*, 1980). A Delaunay triangulation breaks the convex hull of a volume, as defined by a set of points in  $\mathbb{R}^n$ , into a set of primitive shapes called “simplexes”. Each simplex is an n-dimensional triangle.

At each timestep, we compute a Delaunay triangulation for the 16 points defined by corners at  $\{(t_{n-1}, t_n), (\text{lat}_1, \text{lat}_2), (\text{lon}_1, \text{lon}_2), (f_1, f_2)\}$ . Once a Delaunay triangulation has been made, it is a computationally-efficient task to check whether or not an arbitrary new point is within any of the simplexes. We use the Scipy Delaunay implementation, which is based on the open-source *qhull* code (*Barber et al.*, 1996). For any point within the volume, we assign to it the average energy density in  $J/m^3$  within the voxel at the given timestep, multiplied by the average Landau damping factor. Figure 3.6 illustrates the interpolation method.

### Fine-scale frequency interpolation

Our output grid coordinates are given in three dimensions – latitude, longitude, and L-shell. However, our Delaunay construction adds an additional dimension, frequency. We can perform a fine-scale interpolation on the frequency axis by selecting a linearly-spaced grid of sub-frequencies between the two ray frequencies  $f_1, f_2$ . Checking and logging whether or not each new point is within the four-dimensional voxel is equivalent to interpolating and checking in three dimensions, as illustrated in figure 3.7.

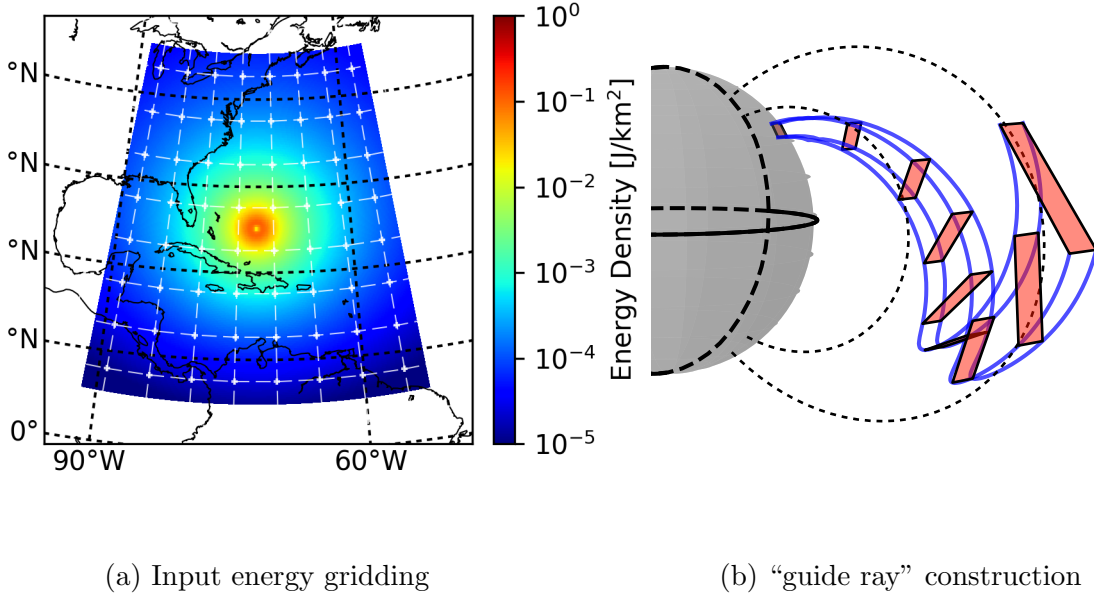


Figure 3.5: An illustration of the interpolation scheme. (a) Energy at the top of the ionosphere is divided into cells, in latitude, longitude, and frequency. Shown here with  $5^\circ$  cells (much larger than used in simulation). The plotted energy is integrated over frequency. (b) Illustration of the guide ray method. Input energy is integrated between a set of guide rays, spaced in latitude, longitude, and frequency. This energy is then averaged over a 4-dimensional volume, bounded by two adjacent timesteps  $t_{n-1}, t_n$  of the guide rays.

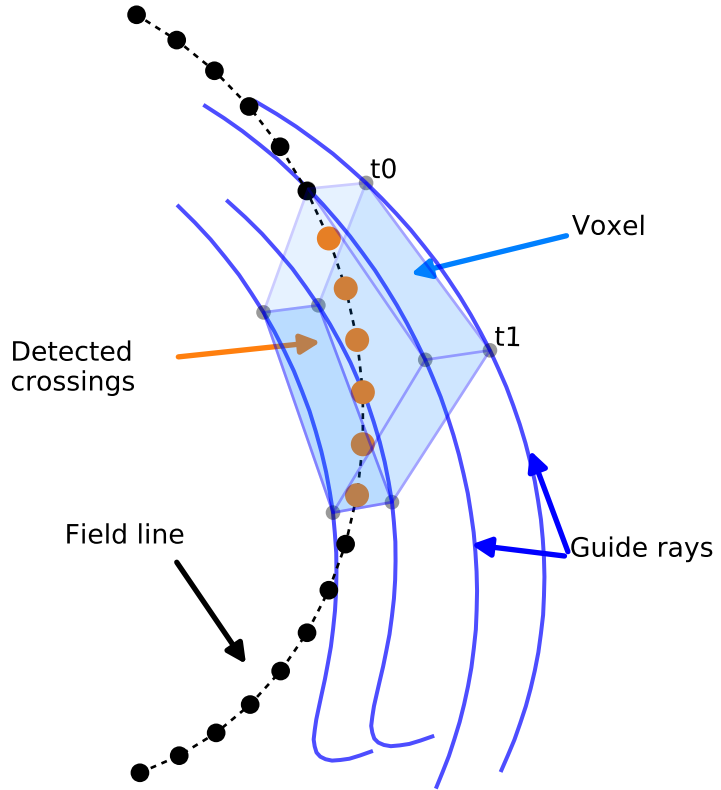


Figure 3.6: Illustration of the Delaunay interpolation method, shown here in three dimensions (e.g., for a single frequency).

## Discussion

Our interpolation method differs substantially from *Bortnik* (2005) and related work. *Bortnik* performed an area-weighted interpolation between guide rays in latitude and frequency, and then looked for ray-segment intersections with cross-sectional areas perpendicular to a field line. Crossings, however, are exceedingly rare over the full set of guide rays and output cross-sectional area segments, which requires clever restriction of the output space, or high computational resources. Our method was selected for computational efficiency when relaxing the meridional-plane restriction,

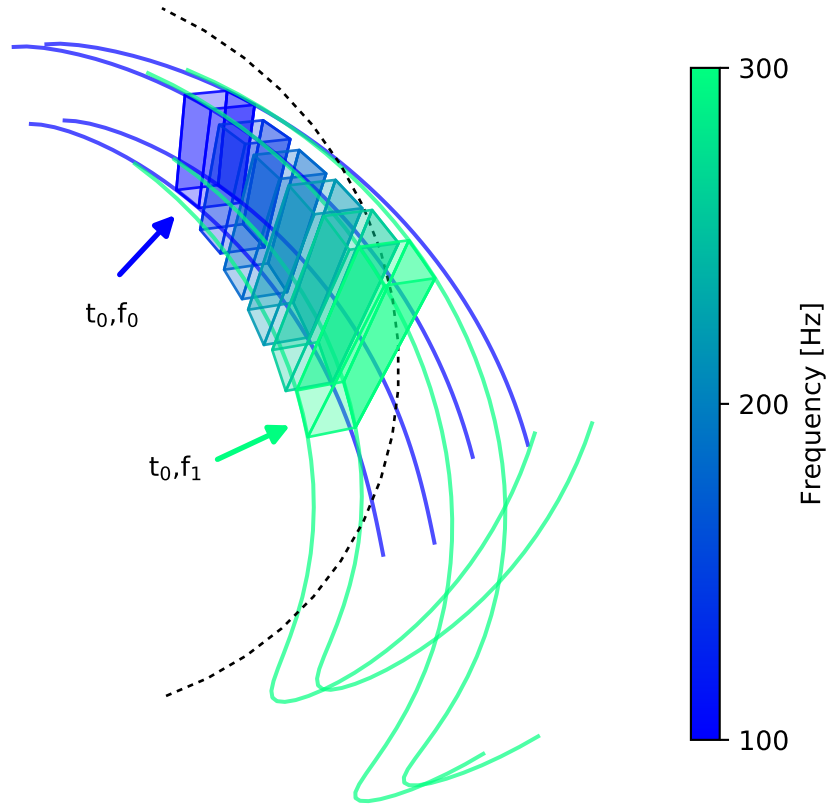


Figure 3.7: An illustration of fine-scale frequency interpolation. Here we show a three-dimensional voxel being linearly interpolated between two sets of guide rays, at  $f_1 = 200$  Hz and  $f_2 = 300$  Hz. Our implementation operates on a four-dimensional voxel, facilitating rapid checking across fine-scale frequency interpolation steps.

and to assure that all input energy is accounted for. Using the *Bortnik* (2005) method with larger intervals in latitude and longitude can result in undersampling the post-ionosphere illumination pattern, while our method integrates the input energy regardless of grid size.

One caveat of our interpolation algorithm is that the Delaunay triangulation implementation only checks whether or not a point is within the convex hull of the

voxel, rather than the voxel itself. For simple voxels, and at early timesteps (e.g., before any magnetospheric reflection), we can be confident that the voxel remains cubic, and the concave and convex hulls are equivalent. However at later timesteps, after the rays have spread and reflected substantially, the concave and convex hulls are likely not equivalent, in which case the interpolation algorithm may artificially disperse the energy over a larger volume, effectively underestimating energy density while overestimating energy spreading. Figure 3.8 shows some simple polygons and their convex hulls.

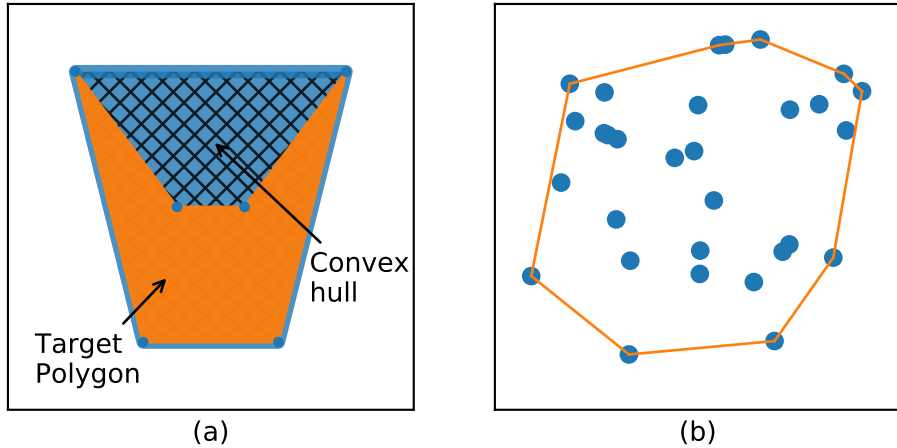


Figure 3.8: Illustration of a convex hull in two dimensions. (a) A simple polygon, shown in orange, for which the convex hull and concave hulls differ substantially. (b) A collection of random points, and their concave hull.

### 3.2.3 Energy imparted by a single flash

The assembled model of a single flash is parameterized by a flash location (latitude, MLT), and  $K_p$ ; the output space can be specified over time, latitude, longitude, L-shell, and frequency. We can reduce the parameter space by integrating over various axes.

Figure 3.9 shows the energy density in the meridional plane, integrated over time and frequency, and averaged over a  $0.25^\circ$  slab in longitude (Note that wave intensity is strongest with a slight offset ( $\sim 100$  km) in longitude – see section 4.2). Energy launched from lower latitudes remains bounded in latitude as it propagates outward; conversely, higher-latitude flashes exhibit more spread in latitude along a fieldline. Higher-latitude flashes also exhibit a stronger “duct-like” enhancement in which energy is well-guided along a fieldline, which we can attribute to the more-gradual curvature of the field line before the first magnetospheric reflection. Lower-latitude flashes encounter stronger field line curvature, and therefore begin to disperse earlier.

Figure 3.10 shows similar data, now volume-averaged over each fieldline, to show the time evolution. In all cases, the most-intense and most-coherent portion of the wave packet disperses within the first  $\sim 3$  seconds. Again, lower-latitude flashes exhibit greater spread in L-shell. Increasing  $K_p$ , which brings the plasmapause closer to the Earth, constrains energy within the plasmasphere, both by reflection from the sharp density gradient, and by increased Landau attenuation due to the increased temperature outside the plasmapause from the thermal model in section 2.5.2. However the closer plasmapause has little effect until at least  $K_p \sim 4$ ; for  $K_p$  values less than 4, the plasmapause remains well above the normal extent of wave energy.

## 3.3 Global Energy Density

In order to estimate the global persistent VLF energy density within the magnetosphere, we first precompute the average energy imparted by a flash at an array of latitudes, for the dayside and nightside, which form our stencil array. We note that our illumination model scales with peak current squared ( $E \propto I_0^2$ ), and that the

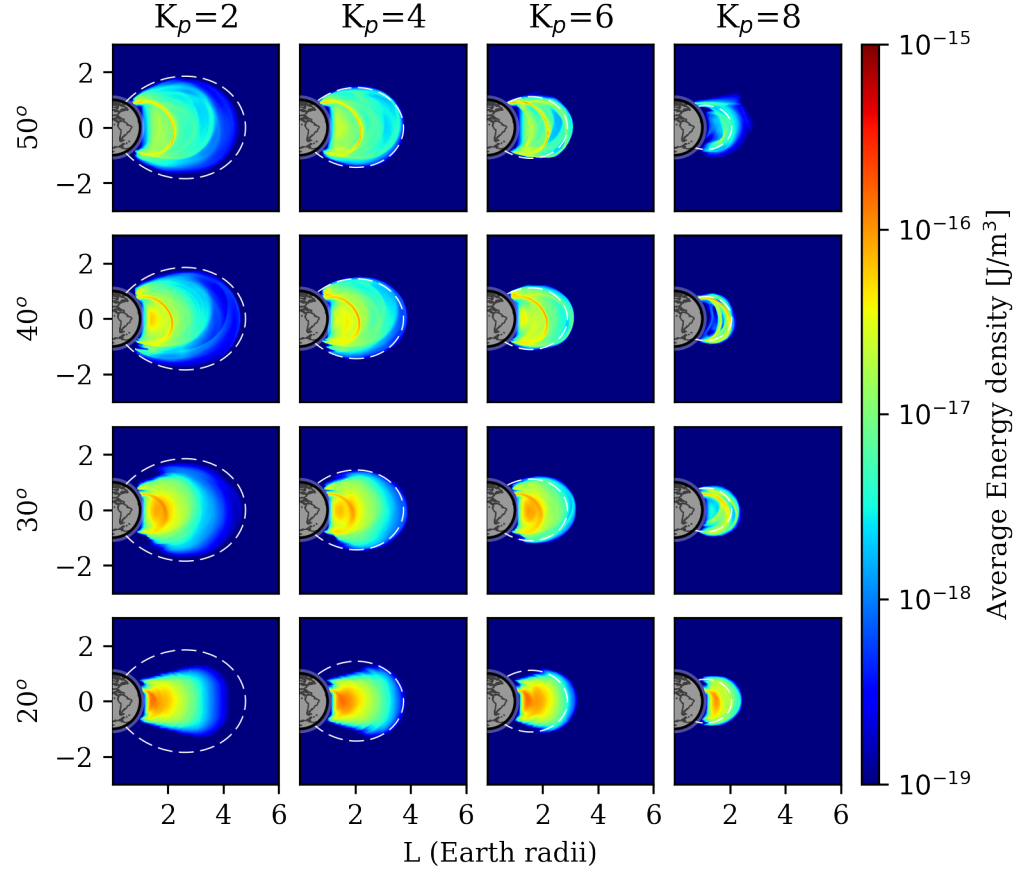


Figure 3.9: Block diagram

propagation process is assumed to be linear – that is, spatially-coincident flashes have no cumulative effect on each other. We can then simply shift and scale our stencils according to lightning measured from GLD360, and sum / average the result.

Stencils are computed for  $1^\circ$  steps, ranging between  $15^\circ$  and  $55^\circ$  in geomagnetic latitude. Noting that the plasmasphere density model is symmetric north / south, and that the magnetic field model is symmetric with the exception of polarity, we assume the impact of a southern hemisphere flash is identical to that of a field-line-coincident northern hemisphere flash. Longitude variation is computed in  $0.25^\circ$  steps, with a maximum extent of  $20^\circ$  from the flash location. We compute stencils for two

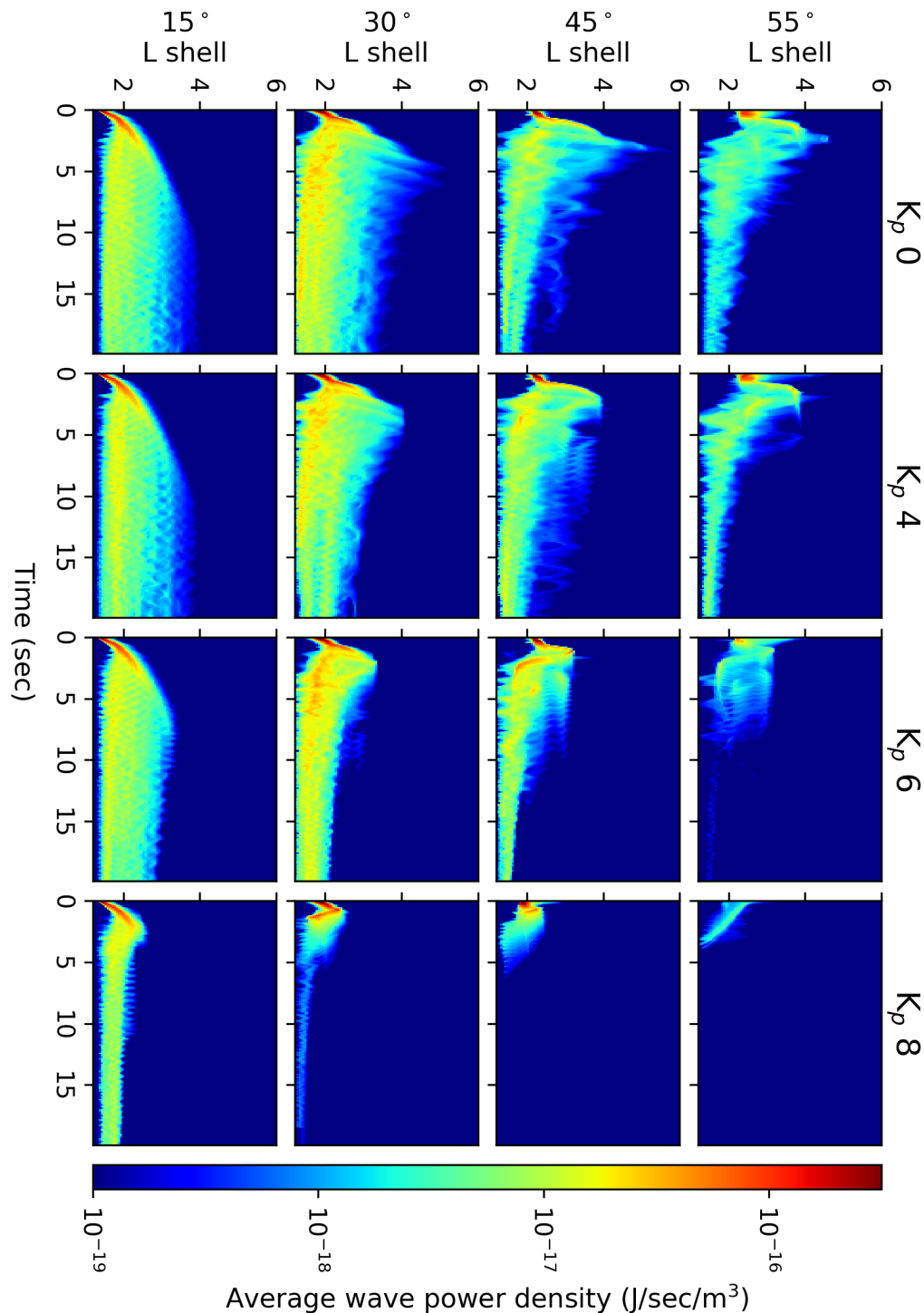


Figure 3.10: Energy density time series plots, for a range of flash latitudes and geomagnetic conditions. Energy is averaged over a  $0.25^\circ$  section in longitude, centered over the flash.

MLT values, 0 and 12, representing the nightside and dayside, and select a stencil set accordingly for each flash. Finally, we compute stencils for an array of  $K_p$  values –  $\{0, 2, 4, 6, 8\}$  – and linearly interpolate along this axis for measured values of  $K_p$ .

Figure 3.11 shows a grid of nightside energy stencils for several latitudes and several  $K_p$ .

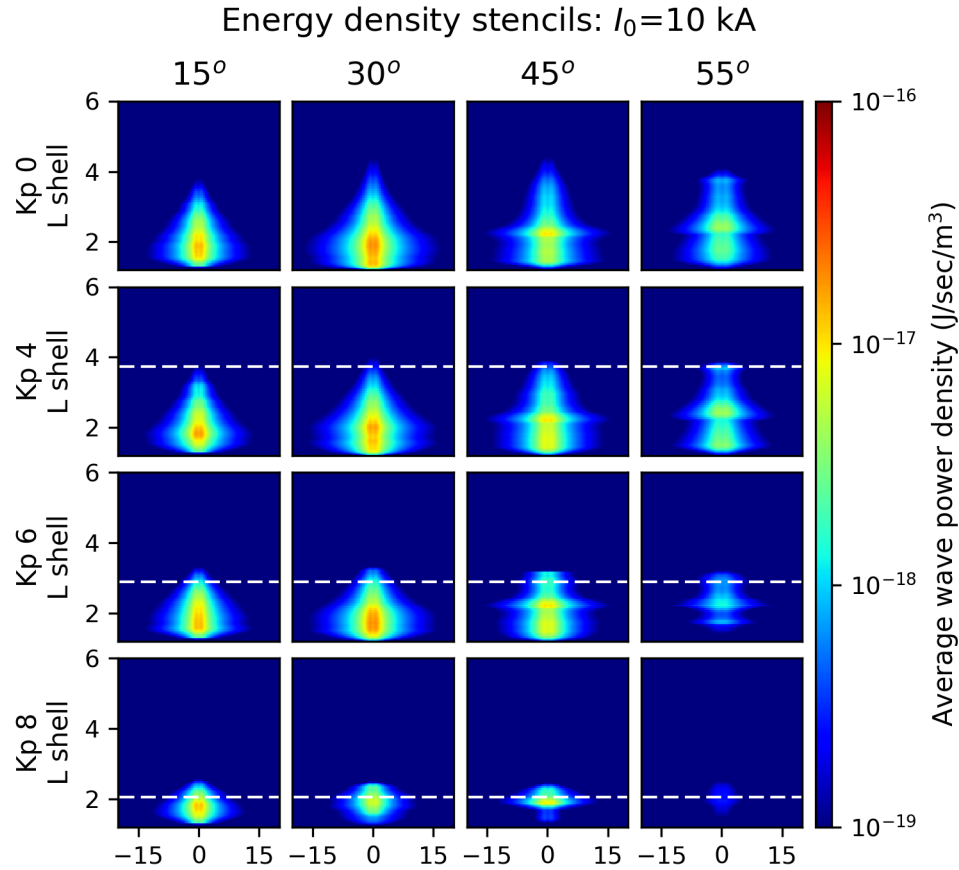


Figure 3.11: Energy density stencils for a range of flash latitudes and geomagnetic conditions, for a nightside, 10 kA flash. The dashed white lines indicate the location of the plasmapause, which is brought closer to the Earth with increasing  $K_p$ .

### 3.3.1 Results of the global model

We apply the shifted and scaled stencil technique to the GLD360 dataset, for all detected flashes between August 2014 and April 2016. Flashes are then binned into dayside and nightside by quantizing magnetic local time:

$$MLT = UT + (\phi_{flash} - \phi_{ut})/15 \quad (3.1)$$

$$\text{Day} \equiv 6 < MLT \leq 18 \quad (3.2)$$

$$\text{Night} \equiv (MLT \leq 6) \parallel (MLT > 18) \quad (3.3)$$

where  $\phi_{flash}$  is the magnetic longitude of the incident flash, UT is the fractional hour of day in universal time, and  $\phi_{ut}$  is the UT reference magnetic longitude of Greenwich (*Laundal and Richmond, 2016*).

We use historical  $K_p$  values corresponding to each flash. However we replace  $K_p$  with  $K_{p(max)}$ , as in *Carpenter and Anderson (1992)*, in order to better align with the plasmasphere model used.  $K_{p(max)}$  is defined as the maximum value of  $K_p$  within the preceding 24-hour period.

Figure 3.12 shows the resulting energy density, averaged over the entire date range, broken out into day and night. Figures 3.13 and 3.14 show the results averaged across the all longitudes.

As shown in figure 3.13, energy density falls off logarithmically with respect to L. The cumulative effect of the plasmapause, the variance of which is taken into effect via multiple  $K_p$  values, results in an additional dropoff at  $L \sim 4.8$ . Energy along the nightside is an order of magnitude greater than the dayside; however outside the plasmapause, day and night are essentially equivalent.

When broken out over  $K_p$  as in figure 3.14, it is apparent that the moving plasmapause location effectively constrains energy to within the inner plasmasphere; however it has little effect on the average energy at lower L-shells, within the inner radiation belt and slot region.

**Frequency dependence** We can examine the frequency spectrum resulting from lightning as a function of L-shell, as shown in figure 3.15. Generally, as seen in figure 2.12, lower-frequency rays propagate further out into the magnetosphere, while higher-frequency rays are strongly-deflected and impact the Earth before a single magnetospheric reflection. This trend results in rays “settling” onto specific fieldlines, dependent on frequency.

The relationship between peak frequency and L-shell is well-defined by a logarithmic fit:

$$\log_{10}(f_{peak}) = 4.56 - 0.48L \quad (3.4)$$

An additional feature of note in figure 3.15 is the broad range of frequencies present at  $L \sim 2.3$ , the location of which strongly supports the hypothesis of lightning as a key mechanism for slot region depletion.

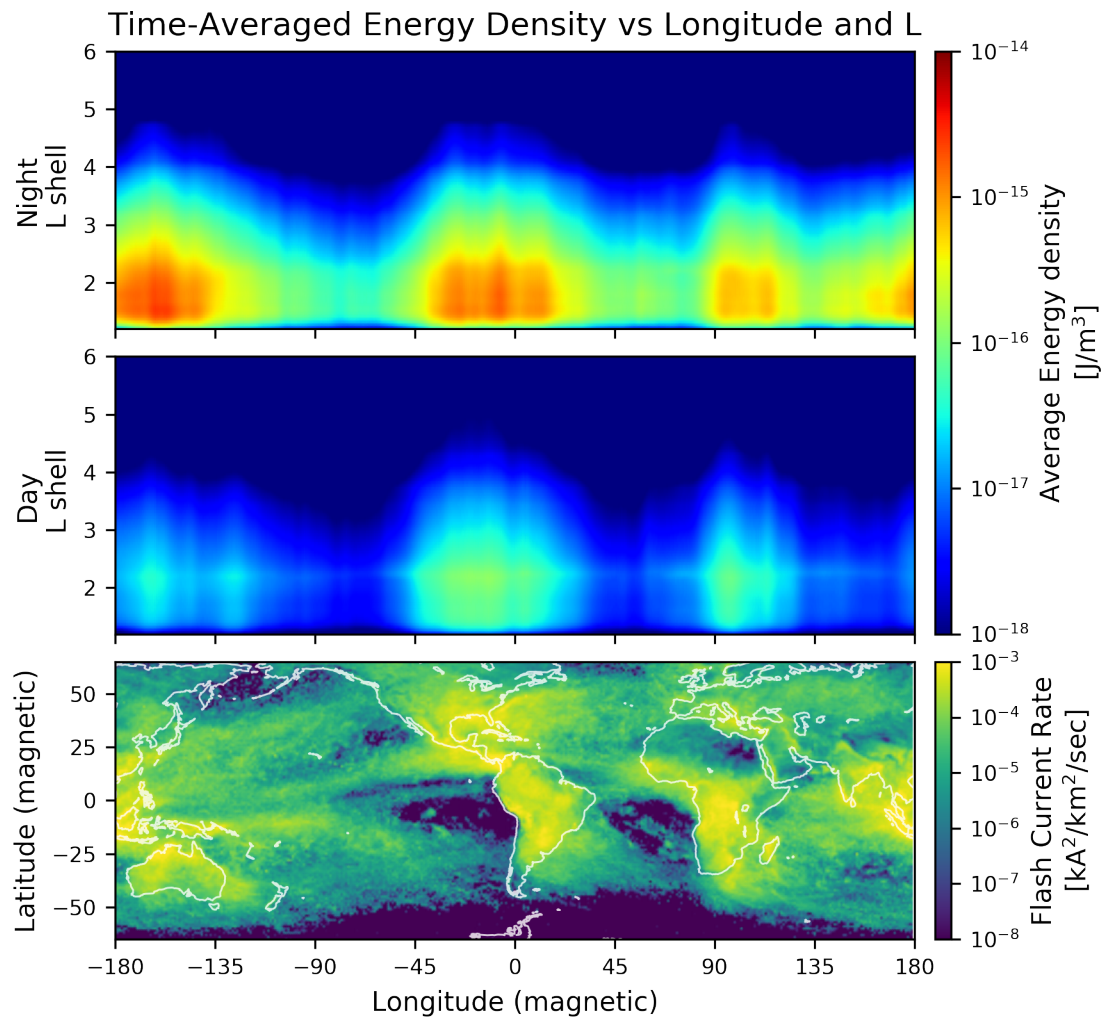


Figure 3.12: Average energy density as a function of L-shell and geomagnetic longitude. The top plot shows the nightside only, and the middle plot shows dayside only. The bottom plot shows the corresponding peak current distribution input into the model.

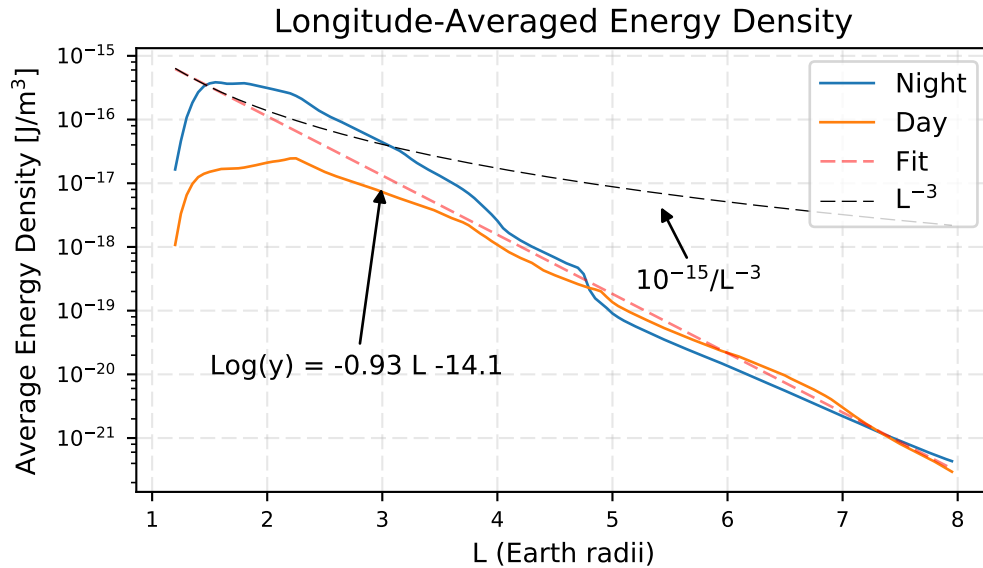


Figure 3.13: Global, longitude-averaged energy density for day and night. The energy density is logarithmic with increasing  $L$ . The dashed black line shows an approximate  $1/R^3$  trend, in comparison with an isotropic radiator.

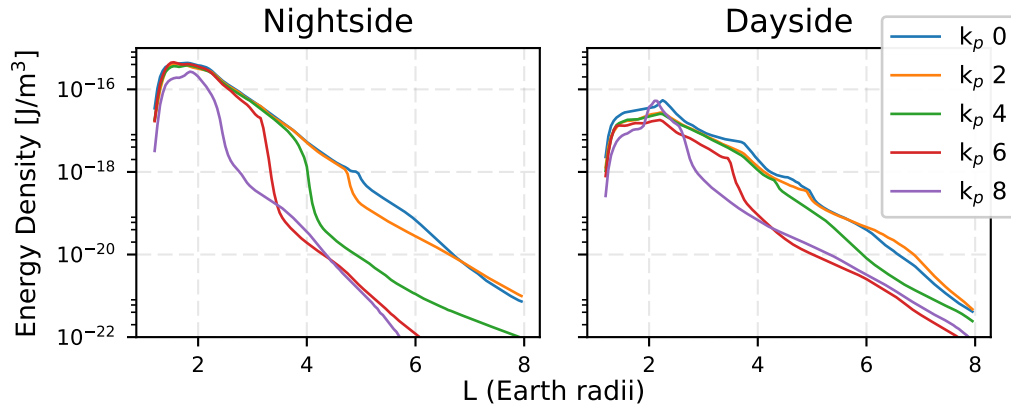


Figure 3.14: Average energy density for day and night, as in figure 3.13, broken out over multiple values of  $K_p$ . At higher  $K_p$ , the plasmapause effectively confines wave energy to the inner plasmasphere.

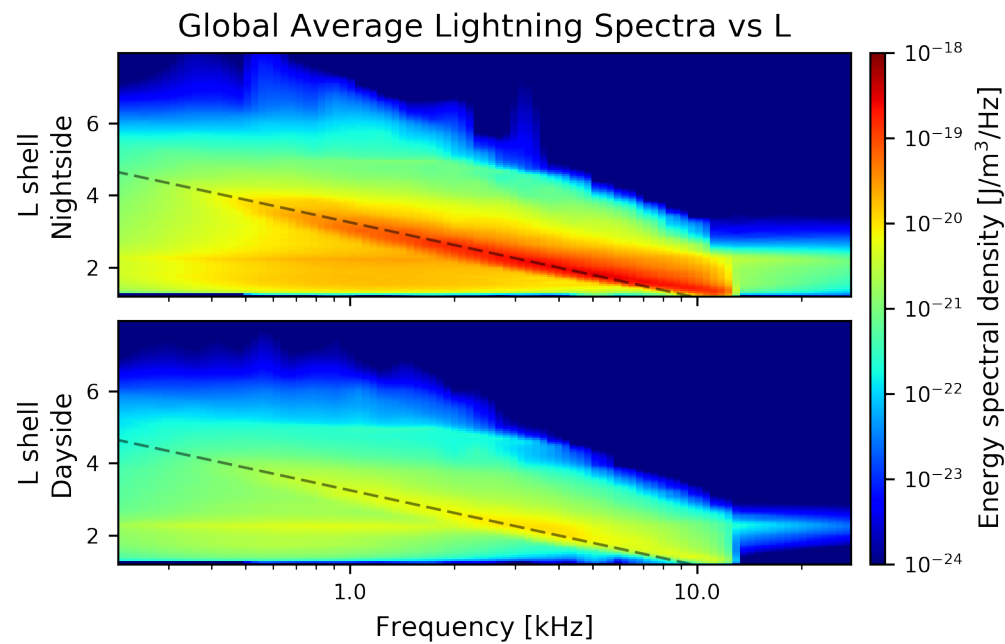


Figure 3.15: Average energy density as a function of L-shell and wave frequency. Dashed lines show a log-linear fit to the peak frequency as a function of L-shell in equation (3.4).

# **Chapter 4**

## **3D Modeling of LEP**

**4.1 Selection of a Canonical Lightning Flash**

**4.2 Pseudo-3D vs Scaled 2D**

**4.3 Geometric Factor**

# Chapter 5

## Global and Seasonal Estimates of LEP

The purpose of this chapter is to provide quantitative upper and lower-bound estimates on the expected electron flux due to LEP, as a function of location and time of year. We expand on the raytracing and interpolation method described in chapter 3, by incorporating a resonant-particle scattering code. We compute global electron fluxes in a similar manner as in chapter 3, using an array of precomputed stencils, which we scale and shift according to GLD360 data. Finally, we can examine the relative timescales on which LEP could deplete a populated magnetic field line, in the absence of any other loss processes.

Where should you put the magnetosphere statistics? that big correlation plot of kp, ae, Dst, etc etc

### 5.1 LEP stencils

### 5.2 Coordinate deformation

The stencils in section 5.1 are computed using a dipole magnetic field, and the simplified GCPM model, both to reduce computational complexity and to better generalize

to multiple longitudes. However, we can approximate the effect of a more-complex magnetic field model via a coordinate transformation, in which we rotate input coordinates to an equivalent dipole-model coordinate, and perform an inverse operation on the stencil output. On the stencil output, this approximation is justified by noting that trapped electrons are bound to their respective field lines, regardless of model used. Justification on the input side (deforming the input coordinates of a lightning flash) is less-concrete, but still a reasonable assumption. First, experimentation with the raytracer reveals that, given a longitudinally-symmetric plasma density model, rays generally follow the longitude deviation of the magnetic field model. Second, while the IGRF and Dipole models differ greatly in its footprint on the ground (as in figure 2.9), within the plasmasphere the two models have reasonable agreement (as in figure 2.8).

The *Corrected Geomagnetic Coordinate* (CGM) (*Hakura*, 1965) system is especially well-suited for this task. CGM coordinates are defined by fieldline tracing between the IGRF and Dipole models. To transform from geographic to CGM coordinates, we first trace a fieldline using IGRF from the surface, up to its intersection with the geomagnetic equatorial plane. We then follow the dipole model back down to the surface, to get an equivalent dipole-model coordinate. The inverse transformation is accomplished by following the dipole field line back up to the equator, and the IGRF model down to its footprint (*Laundal and Richmond*, 2016).

Field line tracing is a computationally-intensive task for a coordinate transformation tool. Historically, researchers relied on precomputed lookup tables and interpolation. The Altitude-Adjusted CGM (AACGM) model (*Baker and Wing*, 1989; *Shepherd*, 2014) uses a spherical-harmonic fit to rapidly transform between CGM and MAG coordinates.

CGM coordinate systems are undefined at some regions near the geomagnetic equator, due to the fact that some IGRF fieldlines may never intersect with it. In these cases, approximate models are often used. *Baker and Wing* (1989) simply omitted geomagnetic latitudes within  $\sim 24^\circ$  of the equator from their study; subsequent researchers have performed spline fits and interpolation to further reduce the undefined region.

We use the algorithm and implementation from *Shepherd* (2014), available at <http://superdarn.thayer.dartmouth.edu/aacgm.html>. Figure 5.1 compares MAG and AACGM contours on a geographic map.

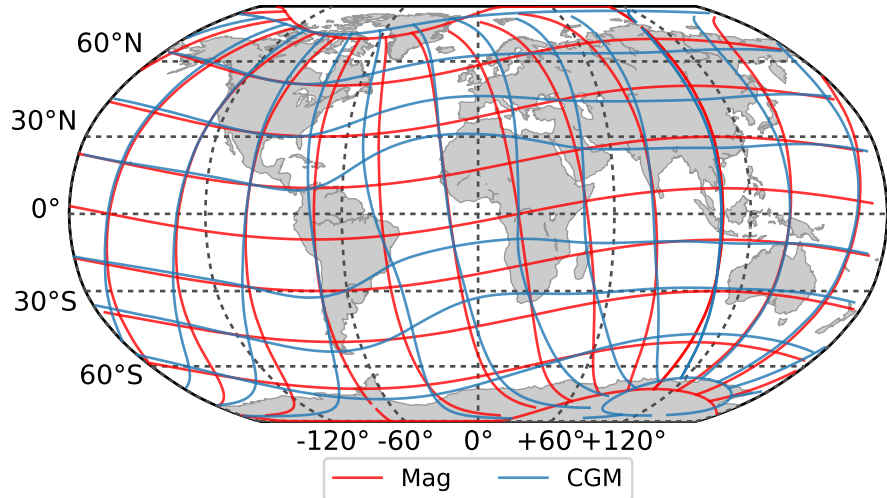


Figure 5.1: A comparison between Magnetic Dipole (MAG) and Corrected Geomagnetic (CGM) coordinates. Corrected Geomagnetic coordinates are obtained by following a magnetic field line, as defined by IGRF, from an input point to its intersection with the magnetic dipole equator. The CGM latitude and longitude are then obtained by following the dipole field line to its footprint on the Earth's surface. Contours are spaced every  $20^\circ$  in geomagnetic latitude, and  $30^\circ$  in geomagnetic longitude.

### 5.3 Global and Seasonal Energy Fluxes

### 5.4 Lifetime Estimates

# **Chapter 6**

## **Satellite Instrumentation for LEP Measurement**

### **6.1 VPM Mission Overview**

### **6.2 Hardware Architecture**

#### **6.2.1 Wave Measurement**

#### **6.2.2 Particle Measurement**

### **6.3 Firmware Architecture**

# Chapter 7

## Conclusions

### 7.1 Suggestions for Future Work

# Appendix A

## Reference Equations

### A.1 Landau Damping

In raytracing, we calculate wave growth and attenuation according to Landau damping. We use the *Brinca* (1972) formulation – itself a reorganization of *Kennel* (1966) – which assumes a cold background plasma, onto which a small thermal electron population is ascribed. The following (frustratingly complex) equation set is taken from *Brinca* (1972), and reprinted here for organization.

Calculating a growth rate begins simply: we assume a time-varying plane wave in the usual complex (“phasor”) form:

$$E \sim E_0 e^{i(\omega t - \mathbf{k} \cdot \mathbf{r})} \quad (\text{A.1})$$

If either  $\omega$  or  $\mathbf{k}$  have an imaginary component, then the result will be an additional real-valued term, which we can factor out as  $\chi$ :

$$E = E_0 e^{i(\omega t - (\mathbf{k}_r + i\mathbf{k}_i) \cdot \mathbf{r})} \quad (\text{A.2})$$

$$= E_0 e^{-\chi r} e^{i(\omega t + \mathbf{k} \cdot \mathbf{r})} \quad (\text{A.3})$$

If the new exponential term  $-\chi$  is positive, the wave will be amplified; if the term is negative, the wave will be attenuated.

The spatial growth rate  $\chi$  is given by equation A.4 (*Brinca*, 1972; *Kennel*, 1966):

$$\chi = -\frac{ck_i}{\omega} = \frac{\delta}{4\eta(2A\eta^2 - B)}(T_1 - T_2 - T_3) \quad (\text{A.4})$$

with the following terms:

$$\begin{aligned} T_1 &= \frac{\eta^2 \sin \theta^2 - P}{2(S - \eta^2)} \Gamma_I \cdot [(R - \eta^2)J_{m-1} + (L - \eta^2)J_{m+1}]^2 G_1 \\ T_2 &= 2[(S - \eta^2 \cos^2 \theta)(S - \eta^2) - D^2] \Lambda_I J_m G_2 \\ T_3 &= 2\eta^2 \sin \theta \cos \theta \Gamma_I \cdot [(R - \eta^2)J_{m-1} + (L - \eta^2)J_{m+1}] G_2 \end{aligned} \quad (\text{A.5})$$

where  $\chi > 0$  indicates damping.

Note that *Brinca* has related the temporal damping rate  $\omega_i$  from *Kennel* (1966) to a spatial damping rate  $k_i$  by assuming a constant propagation at the group velocity  $v_g$ .

$A, B, C, D, L, P, R$ , and  $S$  are the Stix environment parameters given by 2.26 – 2.27, and are functions of wave frequency, local plasma density, and local magnetic field strength.

As previous,  $\theta$  is the angle between the wavenormal vector and the background magnetic field, and  $\eta$  is the wave refractive index, found by solving equation 2.30.

The terms  $J_m$ ,  $J_{m+1}$  and  $J_{m-1}$  are Bessel functions of the first kind, which account for the multiple resonant modes –  $m = 0$  indicates the Landau resonance;  $m \pm 1$  the Cyclotron resonance.

The terms  $\Gamma_I$  and  $\Lambda_I$  are summations over resonant modes  $m \in \{-\infty \dots \infty\}$ , and integrations over the velocity space  $v_\perp, v_\parallel$  given by:

$$\Gamma_I = \frac{2\pi^2\omega_p^2}{\omega k_{\parallel}} \sum_{m=-\infty}^{\infty} \int_0^{\infty} v_{\perp}^2 dv_{\perp} \int_{-\infty}^{\infty} \delta(v_{\parallel} - V_m) dv_{\parallel} \quad (\text{A.6})$$

$$\Lambda_I = \frac{2\pi^2\omega_p^2}{\omega k_{\parallel}} \sum_{m=-\infty}^{\infty} \int_0^{\infty} v_{\perp} dv_{\perp} \int_{-\infty}^{\infty} v_{\parallel} \delta(v_{\parallel} - V_m) dv_{\parallel} \quad (\text{A.7})$$

$$V_m = \frac{\omega - m\omega_c}{k_{\parallel}} \quad (\text{A.8})$$

Finally, the temperature distribution is included in the values  $G_1$  and  $G_2$  – each of which are functions of the *gradient* of the phase-space distribution function:

$$f = f(\mathbf{x}, \mathbf{v}) = f(\mathbf{x}, v_{\perp}, v_{\parallel}):$$

$$G_1 = \left(1 - \frac{k_{\parallel}v_{\perp}}{\omega}\right) \frac{\partial f}{\partial v_{\perp}} + \frac{k_{\parallel}v_{\perp}}{\omega} \frac{\partial f}{\partial v_{\parallel}} \quad (\text{A.9})$$

$$G_2 = J_m \left[ \left(1 + \frac{m\omega_c}{\omega}\right) \frac{\partial f}{\partial v_{\parallel}} - m \frac{\omega_c}{\omega v_{\perp}} \frac{\partial f}{\partial v_{\perp}} \right] \quad (\text{A.10})$$

Despite the complexity of these equations, the phase-space distribution function  $f$  is the only fundamental new input – every remaining parameter is an output of the raytracer, and itself a result of our plasma density and magnetic field models.

Our implementation, derived from *Golden et al.* (2010), computes the gradients of  $f$  numerically using finite differencing, therefore granting the flexibility to use any arbitrary distribution function.

# **Appendix B**

## **Runge-Kutta Methods**

# Bibliography

- Angerami, J. J. (1963), Studies of Planetary Atmospheres 1., *Distribution*, 69(21).
- Appleton, E. V. (1932), Appleton : Wireless Studies of the Ionosphere . Wireless Studies of the Ionosphere .\* Appleton : Wireless Studies of the Ionosphere ., (10).
- Baker, K. B., and S. Wing (1989), A new magnetic coordinate system for conjugate studies at high latitudes, *Journal of Geophysical Research*, 94(A7), 9139, doi: 10.1029/JA094iA07p09139.
- Barber, C. B., D. P. Dobkin, and H. Huhdanpaa (1996), The quickhull algorithm for convex hulls, *ACM Transactions on Mathematical Software*, 22(4), 469–483, doi:10.1145/235815.235821.
- Bell, T. F. (1984), The nonlinear gyroresonance interaction between energetic electrons and coherent VLF waves propagating at an arbitrary angle with respect to the Earth's magnetic field, *Journal of Geophysical Research*, 89(A2), 905–918, doi: 10.1029/JA089iA02p00905.
- Bell, T. F. (2002), The Landau damping of magnetospherically reflected whistlers within the plasmasphere, *Geophysical Research Letters*, 29(15), 2–5, doi: 10.1029/2002GL014752.
- Bilitza, D., and B. W. Reinisch (2008), International Reference Ionosphere 2007: Improvements and new parameters, *Advances in Space Research*, 42(4), 599–609, doi:10.1016/j.asr.2007.07.048.
- Bittencourt, J. A. (2004), *Fundamentals of Plasma Physics*, 3rd ed.

- Blaes, P. R., R. A. Marshall, and U. S. Inan (2016), Global occurrence rate of elves and ionospheric heating due to cloud-to-ground lightning, *Journal of Geophysical Research A: Space Physics*, 121(1), 699–712, doi:10.1002/2015JA021916.
- Bortnik, J. (2005), Precipitation of radiation belt electrons by lightning-generated magnetospherically reflecting whistlers, Ph.D. thesis, Stanford University.
- Bortnik, J., U. S. Inan, and T. F. Bell (2006), Temporal signatures of radiation belt electron precipitation induced by lightning-generated MR whistler waves: 1. Methodology, *Journal of Geophysical Research: Space Physics*, 111(2), 1–22, doi: 10.1029/2005JA011182.
- Bortnik, J., R. M. Thorne, and N. P. Meredith (2007), Modeling the propagation characteristics of chorus using CRRES suprathermal electron fluxes, *Journal of Geophysical Research: Space Physics*, 112(8), 1–13, doi:10.1029/2006JA012237.
- B.Peter, W. (2007), Quantitative Measurement of Lightning-Induced Electron Precipitation Using Vlf Remote Sensing, (February).
- Brinca, A. L. (1972), On the Stability of Obliquely Propagating Whistlers, *Journal of Geophysical Research*, 77(19), 3495–3507.
- Brooks, C. E. P. (1925), The distribution of thunderstorms over the globe, *Geophysical Memorandum*, 24.
- Bruce, C. E. R., and R. H. Golde (1941), The Lightning Discharge, *The Journal of the I.E.E.E*, 88(6), 487–505.
- Carpenter, D. L., and R. R. Anderson (1992), An ISEE / Whistler Model of Equatorial Electron Density in the Magneto sphere Od D ' j :, *J. Geophys. Res.*, 97, 1097–1108.
- Cayton, T. E. (2005), Phase-Space Density Analyses of the AE-8 Trapped Electron and the AP-8 Trapped Proton Model Environments, *Tech. rep.*, Office of Sicientific and Technical Information, Oak Ridge, TN, Los Alamos, NM.

- Chandler, O., M. O. Chandler, J. H. Waite, and T. E. Moore (1991), Observations of polar ion outflows, *Journal of Geophysical Research: Space Physics*, 96(A2), 1421–1428, doi:10.1029/90JA02180.
- Chang, H. C., and U. S. Inan (1983), Quasi-relativistic electron precipitation due to interactions with coherent VLF waves in the magnetosphere, *Journal of Geophysical Research*, 88(A1), 318–328.
- Chen, F. F. (1983), *Introduction to Plasma Physics and Controlled Fusion*, Plenum Press, New York, NY, doi:QC718.C39 1983.
- Cohen, M. B., N. G. Lehtinen, and U. S. Inan (2012), Models of ionospheric VLF absorption of powerful ground based transmitters, *Geophysical Research Letters*, 39(24), 1–5, doi:10.1029/2012GL054437.
- Cotts, B. R. T. (2011), Global Quantification of Lightning-Induced Electron Precipitation Using Very Low Frequency Remote Sensing, Ph.D. thesis.
- Delaunay, B. (1934), Sur la sphere vide, doi:10.1051/jphysrad:01951001207073500.
- Edgar, B. (1972), The structure of the magnetosphere as deduced from magnetospherically reflected whistlers, Ph.D. thesis, Stanford University.
- Fehlberg, E. (1969), Low-order classical Runge-Kutta formulas with stepsize control and their application to some heat transfer problems, *Tech. Rep. July*, NASA.
- Gallagher, D. L., P. D. Craven, R. H. Comfort, and T. E. Moore (1995), On the azimuthal variation of core plasma in the equatorial magnetosphere, *Journal of Geophysical Research: Space Physics*, 100(A12), 23,597–23,605, doi:10.1029/95JA02100.
- Gallagher, D. L., P. D. Craven, and R. H. Comfort (1999), Global Core Plasma Model, *Journal of Geophysical Research: Space Physics*, 105(A8), 18,819–18,833, doi:10.1029/1999JA000241.

- Golden, D. I., M. Spasojevic, F. R. Foust, N. G. Lehtinen, N. P. Meredith, and U. S. Inan (2010), Role of the plasmapause in dictating the ground accessibility of ELF/VLF chorus, *Journal of Geophysical Research: Space Physics*, 115(11), 1–15, doi:10.1029/2010JA015955.
- Graf, K. L., N. G. Lehtinen, M. Spasojevic, M. B. Cohen, R. A. Marshall, and U. S. Inan (2013), Analysis of experimentally validated trans-ionospheric attenuation estimates of VLF signals, *Journal of Geophysical Research: Space Physics*, 118(5), 2708–2720, doi:10.1002/jgra.50228.
- Griffiths, D. J. (1999), *Introduction to Electrodynamics*, 3rd ed., Prentice-Hall, Inc, Upper Saddle River, New Jersey.
- Hakura, Y. (1965), Tables and maps of geomagnetic coordinates corrected by the higher spherical harmonic terms, *Rep. Ionos. Space Res. Japan*, 19, 121–157.
- Haselgrove, J. (1954), Ray theory and a new method for ray tracing, *Report of the Physical Society Conference on Physics of the Ionosphere*, pp. 355–364.
- Haselgrove, J., and C. B. Haselgrove (1960), Twisted ray paths in the ionosphere, *Proceedings of the Physical Society*, 75, 357–363, doi:10.1088/0370-1301/70/7/302.
- Helliwell, R. A. (1965), *Whistlers and Related Ionospheric Phenomena*, Stanford University Press.
- Henyey, F. S. (1980), Improved ray description of wave equations, *Physical Review Letters*, 45(24), 1897–1900, doi:10.1103/PhysRevLett.45.1897.
- Horner, F. (1954), The accuracy of the location of sources of atmospherics by radio direction-finding, *Proceedings of the IEE - Part III: Radio and Communication Engineering*, 101(74), 383–390, doi:10.1049/pi-3.1954.0091.
- Horner, F. (1957), Very-Low-Frequency Propagation and Direction-Finding, *The Proceedings of the Institution of Electrical Engineers*, 104(14), 73–80.

- Jasna, R.-D. L. (1993), Gyroresonant Scattering of Radiation Belt Electrons by Oblique Whistler Waves, Ph.D. thesis, Stanford University.
- Kennel, C. (1966), Low-Frequency Whistler Mode, *Physics of Fluids*, 9(11), 2190, doi:10.1063/1.1761588.
- Kimura, I. (1966), Effects of Ions on Whistler-Mode Ray Tracing, *Radio Science*, 1(3), 269–283, doi:10.1002/rds196613269.
- Krider, E. P., R. C. Noggle, A. E. Pifer, and D. L. Vance (1980), Lightning Direction-Finding Systems for Forest Fire Detection, doi:10.1175/1520-0477(1980)061j0980:LDFSFF;2.0.CO;2.
- Kulkarni, P. (2009), Controlled precipitation of radiation belt electrons, Ph.D. thesis, Stanford University, doi:10.1029/2002JA009580.
- Landau, L. D. (1946), On the vibrations of the electronic plasma, *Soviet Journal of Physics*.
- Lauben, D. (1998), Precipitation of radiation belt Electrons by obliquely-propagating lightning-generated whistler waves, Ph.D. thesis, Stanford University.
- Laundal, K. M., and A. D. Richmond (2016), Magnetic Coordinate Systems, *Space Science Reviews*, pp. 1–33, doi:10.1007/s11214-016-0275-y.
- Lee, D. T., and B. J. Schachter (1980), Two algorithms for constructing a Delaunay triangulation, *International Journal of Computer & Information Sciences*, 9(3), 219–242, doi:10.1007/BF00977785.
- Marshall, R. A., J. Bortnik, N. Lehtinen, and S. Chakrabarti (2011), Optical signatures of lightning-induced electron precipitation, *Journal of Geophysical Research: Space Physics*, 116(8), 1–8, doi:10.1029/2011JA016728.
- Mathews, J. H., and K. D. Fink (2004), *Numerical Methods Using Matlab*.

- McIlwain, C. E. (1961), Coordinates for mapping the distribution of magnetically trapped particles, *Journal of Geophysical Research*, 66(11), 3681–3691, doi: 10.1029/JZ066i011p03681.
- Nag, A., S. Mallick, V. A. Rakov, J. S. Howard, C. J. Biagi, J. D. Hill, M. A. Uman, D. M. Jordan, K. J. Rambo, J. E. Jerauld, B. A. DeCarlo, K. L. Cummins, and J. A. Cramer (2011), Evaluation of U.S. national lightning detection network performance characteristics using rocket-triggered lightning data acquired in 2004–2009, *Journal of Geophysical Research Atmospheres*, 116(2), 1–8, doi: 10.1029/2010JD014929.
- Ngo, H. D. (1989), Electrostatic waves stimulated by VLF whistler mode waves scattering from magnetic-field-aligned plasma density irregularities, Ph.D. thesis, Stanford University.
- Orville, R. E. (1995), Lighting Detection from Ground and Space, in *Handbook of Atmospheric Electrodynamics*, pp. 137–149.
- Orville, R. E., and D. W. Spencer (1979), Global Lightning Flash Frequency, doi: 10.1175/1520-0493(1979)107j0934:GLFF;2.0.CO;2.
- Persoon, A. M., D. A. Gurnett, and S. D. Shawhan (1983), Polar cap electron densities from DE 1 plasma wave observations, *Journal of Geophysical Research: Space Physics*, 88(A12), 10,123–10,136, doi:10.1029/JA088iA12p10123.
- Said, R. K., U. S. Inan, and K. L. Cummins (2010), Long-range lightning geolocation using a VLF radio atmospheric waveform bank, *Journal of Geophysical Research: Atmospheres*, 115(23), 1–19, doi:10.1029/2010JD013863.
- Sazhin, S. (1993), *Whistler-mode Waves in a Hot Plasma*, 1 ed., Cambridge University Press, Cambridge.
- Shepherd, S. G. (2014), Altitude-adjusted corrected geomagnetic coordinates: Definition and functional approximations, *Journal of Geophysical Research: Space Physics*, 119(9), 7501–7521, doi:10.1002/2014JA020264.

- Starks, M. J., R. A. Quinn, G. P. Ginett, J. M. Albert, G. S. Sales, B. W. Reinisch, and P. Song (2008), Illumination of the plasmasphere by terrestrial very low frequency transmitters: Model validation, *Journal of Geophysical Research: Space Physics*, 113(9), 1–16, doi:10.1029/2008JA013112.
- Stix, T. H. (1992), *Waves in Plasmas*, American Institute of Physics, New York, NY, doi:QC718.5.W3S75.
- Thébault, E., C. C. Finlay, C. D. Beggan, P. Alken, J. Aubert, O. Barrois, F. Bertrand, T. Bondar, A. Boness, L. Brocco, E. Canet, A. Chambodut, A. Chuliat, P. Coisson, F. Civet, A. Du, A. Fournier, I. Fratter, N. Gillet, B. Hamilton, M. Hamoudi, G. Hulot, T. Jager, M. Korte, W. Kuang, X. Lalanne, B. Langlais, J.-M. Léger, V. Lesur, F. J. Lowes, S. Macmillan, M. Mandea, C. Manoj, S. Maus, N. Olsen, V. Petrov, V. Ridley, M. Rother, T. J. Sabaka, D. Saturnino, R. Schachtschneider, O. Sirol, A. Tangborn, A. Thomson, L. Tøffner-Clausen, P. Vigneron, I. Wardinski, and T. Zvereva (2015), International Geomagnetic Reference Field: the 12th generation, *Earth, Planets and Space*, 67(1), 79, doi: 10.1186/s40623-015-0228-9.
- Tsyganenko, N. A., and M. I. Sitnov (2005), Modeling the dynamics of the inner magnetosphere during strong geomagnetic storms, *Journal of Geophysical Research: Space Physics*, 110(A3), 1–16, doi:10.1029/2004JA010798.
- Van Allen, J. A. (1958), Observation of High Intensity Radiation by Satellites 1958 Alpha and Gamma, *Journal of Jet Propulsion*, 28(9), 588–592, doi:10.2514/8.7396.
- Vette, I. (1991), The Model Trapped Electron Environment, *Environment*.
- Vette, J. I. (1966), Models of the Trapped Radiation environment: Volume I: Inner Zone Protons and Electrons, *Tech. rep.*, Scientific and Technical Information Division; National Aeronautics and Space Administration (NASA).